This is a non-peer reviewed preprint submitted to EarthArXiv.
This manuscript has been submitted for peer review.

Subsequent versions may have altered content.

Please contact Vince Cooper (vcooper@uw.edu) regarding this manuscript's content.

PNAS

Main Manuscript for

Last Glacial Maximum pattern effects reduce climate sensitivity estimates

Vincent T. Cooper[a,*], Kyle C. Armour[a,b], Gregory J. Hakim[a], Jessica E. Tierney[c], Matthew B. Osman[d], Cristian Proistosescu[e], Yue Dong[f], Natalie J. Burls[g], Timothy Andrews[h], Daniel E. Amrhein[i], Jiang Zhu[i], Wenhao Dong[j], Yi Ming[k], and Philip Chmielowiec[e]

[a] Department of Atmospheric Sciences, University of Washington, Seattle, WA, USA
[b] School of Oceanography, University of Washington, Seattle, WA, USA
[c] Department of Geosciences, University of Arizona, Tucson, AZ, USA
[d] Department of Geography, University of Cambridge, UK
[e] Department of Atmospheric Sciences and Department of Geology, University of Illinois at Urbana Champaign, Urbana, IL, USA
[f] Lamont-Doherty Earth Observatory, Columbia University, Palisades, NY, USA
[g] Department of Atmospheric, Oceanic, and Earth Sciences, George Mason University, Fairfax, VA, USA
[h] Met Office Hadley Centre, Exeter, UK
[i] Climate and Global Dynamics Laboratory, National Center for Atmospheric Research, Boulder, CO, USA
[j] NOAA/Geophysical Fluid Dynamics Laboratory, Princeton, NJ, USA
[k] Earth and Environmental Sciences and Schiller Institute for Integrated Science and Society, Boston College, Boston, MA, USA

*Corresponding author: Vincent T. Cooper

Email: vcooper@uw.edu

Author Contributions: V.T.C. performed the analysis, designed the simulations, wrote the original draft, and ran the simulations in CAM5 and CAM4; K.C.A. initiated the study with support from G.J.H., C.P., J.E.T, and N.J.B; K.C.A. and G.J.H. supervised the research; G.J.H., J.E.T., M.B.O., and D.E.A. contributed expertise on data assimilation and LGM reconstructions; Y.D., N.J.B., T.A., C.P., J.Z., and Y.M. contributed to analysis and interpreting results; T.A. ran AGCM simulations in HadGEM3-GC3.1-LL, W.D. in GFDL-AM4, and P.C. in CAM6; J.Z. provided coupled simulations in CESM; all authors contributed to editing the paper.

Competing Interest Statement: The authors declare no competing interests.

Classification: Physical Sciences/Earth, Atmospheric, and Planetary Sciences.

Keywords: Climate change, climate sensitivity, paleoclimate, climate feedbacks, pattern effect

This PDF file includes:

Main Text
Figures 1 to 4

Abstract

The Last Glacial Maximum (LGM) provides a leading constraint on equilibrium climate sensitivity (ECS), a measure of global-mean warming from increased greenhouse gas concentrations. Feedbacks governing climate sensitivity depend on the spatial pattern of sea-surface temperature (SST), a phenomenon known as the "pattern effect." Using the LGM to constrain future warming requires accurately reconstructing SST patterns and quantifying how feedbacks differ between the LGM and modern-day. Here we show that the climate is more sensitive to LGM forcing than modern-day CO_2 because LGM ice-sheet forcing amplifies SST changes in the extratropics where feedbacks are less stabilizing. We quantify this LGM pattern effect using atmospheric models combined with spatially complete LGM SST reconstructions from paleoclimate data assimilation projects. Revising modern-day ECS to account for LGM pattern effects results in stronger constraints. Combining the LGM with other lines of evidence, we find a modern-day ECS of 2.9°C (2.1–4.1°C, 5–95% range), substantially narrowing uncertainty compared to recent community assessments that did not account for LGM pattern effects. Our results demonstrate the importance of accounting for pattern effects when inferring ECS from paleoclimate periods affected by substantial non-CO_2 forcing.

Significance Statement

Paleoclimates provide examples of past climate change that inform estimates of modern warming from greenhouse gases. However, paleoclimate evidence can be misleading if differences between the past and present climates are not accounted for. We show that global cooling at the peak of the last ice age was amplified by the presence of massive ice sheets (covering much of North America) through their impact on the spatial pattern of sea-surface temperature. Because these ice sheets are not present today and will not play any role in amplifying modern warming, the expected warming from carbon dioxide is less than previously thought, and uncertainty is substantially reduced.

Main Text

Introduction

Equilibrium climate sensitivity (ECS) is the steady-state response of global-mean near-surface air temperature to doubling atmospheric CO_2 above pre-industrial levels. ECS is a focus of climate policy and projections because it governs Earth's long-term response to anthropogenic greenhouse gas changes (1, 2) . Recently, the World Climate Research Programme's 2020 climate sensitivity assessment, hereafter "WCRP20" (1), updated the 5–95% range for ECS to 2.3–4.7°C with a central estimate of 3.1°C, which informed the *very likely* range of 2.0–5.0°C and central estimate of 3°C in the Intergovernmental Panel on Climate Change Sixth Assessment Report ("IPCC AR6") (2). This narrowing of uncertainty compared to previous assessments was achieved by quantitatively combining evidence from process understanding of climate feedbacks, observations over the historical record (1870–present), and paleoclimate reconstructions of past cold and warm periods. Of these lines of evidence, paleoclimate data from the Last Glacial Maximum (LGM), approximately 21,000 years ago, provide a leading constraint on the upper bound of ECS (1–3).

Using paleoclimate data to constrain modern-day ECS requires accounting for how climate feedbacks change across different climate states (1, 2, 4–9). The standard assumption is that colder climates are less sensitive (i.e., have more-negative feedbacks) than warmer states (1, 2, 5–9). However, the simple assumption that feedbacks change with *global-mean* temperature does not account for how feedbacks depend on changing *spatial patterns* of sea-surface temperature (SST), a phenomenon known as the SST "pattern effect" (10–15).

A robust understanding of the SST pattern effect has been developed in the context of recent warming. Over the past century, SSTs have warmed more in the tropical west Pacific and less in the east Pacific and Southern Ocean (12, 16, 17). SST changes in tropical regions of deep convection (e.g., the west Pacific) produce strongly negative (stabilizing) feedbacks, whereas SST changes in regions with reflective low clouds (e.g., the east Pacific) or sea ice produce relatively positive (destabilizing) feedbacks (11–15, 18). This historical pattern of SST trends is expected to reverse in the future as the tropical east Pacific and Southern Ocean eventually warm at higher rates, producing more-positive feedbacks and a more-sensitive climate (15, 19, 20). Accounting for pattern effects causes the historical record to become a weak constraint on high values of ECS (1, 2, 16, 17), leaving the LGM as a leading constraint on the ECS upper bound (1).

However, pattern effects have not been accounted for in LGM evidence for modern-day ECS (1–3, 5, 21). Importantly, if the spatial pattern of SST change at the LGM differs from the pattern of future warming, then the climate feedbacks governing climate sensitivity will differ as well. Continental ice sheets are responsible for approximately half of the total LGM forcing (3, 22, 23) and drive distinct climate responses from changes in topography, albedo, and sea-level (22, 24–29), suggesting that patterns of SST change at the LGM may differ substantially from those in response to a modern-day doubling of CO_2. Previous work acknowledged this possibility (1, 2) but did not account for LGM pattern effects because no quantification had yet been made. A key question is, would accounting for LGM pattern effects strengthen or weaken constraints on modern-day ECS?

Here we provide the first quantification of the LGM pattern effect and its uncertainty by leveraging two recent advances. First, with the advent of paleoclimate data assimilation (30), spatially complete reconstructions of SST and sea ice now exist for the LGM (3, 31–33), including estimated uncertainties. Second, recent progress in quantifying pattern effects (16, 17) provides methods using atmospheric general circulation models (AGCMs) to link SST patterns to climate feedbacks. These advances present a new opportunity to compare SST changes at the LGM with those expected under anthropogenic CO_2 forcing and to quantify resulting differences in climate feedbacks and sensitivity. To assess the robustness of our results, we use five AGCMs (sampling uncertainty in how feedbacks relate to SST patterns) and four reconstructions (3, 31–33) of the LGM (sampling uncertainty in SST patterns).

Dependence of modern-day ECS on pattern effects

ECS and climate feedbacks are connected through the standard model of global-mean energy balance:

$$\Delta N = \lambda \Delta T + \Delta F, \quad [1]$$

where N is the top-of-atmosphere radiative imbalance; λ is the net climate feedback (negative for stable climates); T is the near-surface air temperature; and F is the "effective" radiative forcing, i.e., the change in net downward radiative flux after adjustments to imposed perturbations but excluding radiative responses to changing surface temperature (1, 2). Differences (Δ) are relative to an equilibrium reference state, e.g., the pre-industrial period. When the forcing is a CO_2-doubling ($2xCO_2$) of pre-industrial values, and the climate system reaches equilibrium ($\Delta N=0$), the resulting ΔT is referred to as the ECS:

$$\mathrm{ECS} = -\Delta F_{2x}/\lambda_{2x}, \quad [2]$$

where ΔF_{2x} is the effective radiative forcing, and λ_{2x} is the net feedback for $2xCO_2$. More-negative values of λ_{2x} indicate a less-sensitive climate (lower ECS).

Here we aim to quantify the difference in feedbacks ($\Delta\lambda$) operating in the modern climate under $2xCO_2$ (λ_{2x}) and at the LGM (λ_{LGM}):

$$\Delta\lambda = \lambda_{2x} - \lambda_{LGM}. \quad [3]$$

Following recent research on pattern effects in the historical record (1, 16, 17), we estimate λ_{2x} and λ_{LGM} using AGCM simulations with SST and sea-ice concentration (SIC) prescribed as surface boundary conditions. We further evaluate the contributions to $\Delta\lambda$ from pattern effects and global-mean temperature changes between the LGM and $2xCO_2$.

To infer the modern-day ECS from LGM evidence, equations (2) and (3) can be combined (1, 16) to yield

$$\mathrm{ECS} = -\Delta F_{2x} / (\lambda^*_{\mathrm{LGM}} + \Delta\lambda), \qquad [4]$$

where λ^*_{LGM} is the estimate of the unadjusted LGM feedback (determined using Eq. 1 applied to that state), which we take from previous assessments (1–3), and $\Delta\lambda$ is estimated from our AGCM simulations. The value of $\Delta\lambda$ depends on spatial patterns of LGM SST and SIC anomalies, for which we use state-of-the-art reconstructions (3, 31–33) based on data assimilation.

From data assimilation to pattern effects

Similar to Bayesian statistics, paleoclimate data assimilation (30) begins with a "prior" estimate of the climate state from model ensembles. Proxy data provide indirect climate observations that update the prior, balancing relative error in the prior and the observations. This results in a "posterior" state estimate, constrained by observations and accounting for uncertainty in priors and data. Since the posterior is sensitive to priors, proxies, and methods, we sample this uncertainty (34) by using multiple reconstructions.

Figure 1 shows the four SST reconstructions (Materials and Methods) we use to quantify the LGM pattern effect. All four reconstructions have a prominent common feature: amplified extratropical cooling in both the North Pacific and North Atlantic Oceans. While the LGM reconstructions differ in other regions that are important for climate feedbacks, e.g., the tropical Pacific (11–15) and Southern Ocean (19, 35, 36), their robust agreement in the northern extratropics proves to be essential for the LGM pattern effect. The zonally consistent maximum near 40°N in SST anomalies at the LGM is in strong contrast to the near-equilibrium response to modern-day $2xCO_2$ (Fig. 1F; SI Appendix, Fig. S1) as simulated by climate models in LongRunMIP (37) (Materials and Methods), suggesting the potential for feedbacks to differ between LGM and $2xCO_2$ climates. Using data-constrained patterns to quantify how LGM feedbacks compare to feedbacks in $2xCO_2$ is a major advance over past comparisons (all based on models), which have produced conflicting results (21, 22, 38–42) (SI Appendix, Text S1).

We calculate net feedbacks using AGCMs with prescribed SST and SIC boundary conditions. We first conduct AGCM simulations with a "baseline" pattern representing the pre-industrial climate, for which we use SST and SIC in the Late Holocene (mean of 0–4,000 years ago) from the Last Glacial Maximum Reanalysis (31) (LGMR). We then perform AGCM simulations with SST and SIC boundary conditions (Materials and Methods) from $2xCO_2$ in LongRunMIP (37) and the four LGM reconstructions (3, 31–33) (SST in Fig. 1; SIC in SI Appendix, Fig. S2). Finally, we calculate global-mean ΔN and ΔT in each $2xCO_2$ and LGM simulation relative to the baseline, which yields net feedbacks as $\lambda = \Delta N/\Delta T$ using Eq. 1. All forcings are held constant ($\Delta F=0$) at modern-day levels across our AGCM simulations, therefore all changes in simulated top-of-atmosphere radiation and feedbacks can be attributed solely to SST/SIC differences (Materials and Methods).

We find that λ_{2x} is more negative (stabilizing) than λ_{LGM}, indicating that the climate system is more sensitive to LGM forcing than to $2xCO_2$ (Fig. 2). We use the LGMR pattern (Fig. 1A) in five AGCMs (CAM4, CAM5, CAM6, GFDL-AM4, and HadGEM3-GC3.1-LL) to evaluate uncertainty from atmospheric model physics, and we use all four LGM reconstructions (Fig. 1A–D) in CAM4 and CAM5 to evaluate uncertainty from LGM patterns. The LGM pattern effect, $\Delta\lambda$ in Eq. 3, is negative across all five AGCMs and all four LGM reconstructions. The five AGCMs produce a mean $\Delta\lambda = -0.40$ $\mathrm{Wm^{-2}K^{-1}}$ (Fig. 2B; detailed results in SI Appendix, Tables S1–S2). We also evaluate uncertainty in the $2xCO_2$ pattern but find that this is of secondary importance (Materials and Methods; SI Appendix, Figs. S3–S4). Our main result is that the climate is more sensitive to LGM forcing than it is to modern-day $2xCO_2$ forcing ($\Delta\lambda<0$), implying lower estimates of modern-day ECS by Eq. 4, and this finding is robust despite uncertainties in atmospheric physics and LGM reconstructions.

Physical mechanisms driving LGM pattern effects

For comparison with our feedbacks in AGCMs driven by LGM reconstructions, we examine previously published results (22) from AGCMs coupled to mixed-layer ("slab") oceans (Fig. 2), which allow SST changes in response to imposed forcings but exclude changes in ocean dynamics (43). These mixed-layer-model versions of CESM1-CAM5 (22), CESM2-CAM6 (44), and CESM2-PaleoCalibr (45) (using a modified CAM6), which differ from our AGCM experiments by including forcings from ice sheets and greenhouse gases, also produce $\Delta\lambda<0$. Although disagreements in SST patterns compared to proxy data suggest that free-running coupled models cannot reliably estimate the value of $\Delta\lambda$, the models demonstrate the physical mechanisms linking patterns of forcing, SST response, and climate feedbacks.

Comparing zonal-mean patterns of effective radiative forcing and SST changes from CESM1-CAM5 simulations (22) under $2xCO_2$ forcing, LGM forcing (ice sheets and greenhouse gases), and LGM ice-sheet forcing alone (including coastline changes) demonstrates that localized ice-sheet forcing causes the amplified SST response in the northern extratropics at the LGM compared to $2xCO_2$ (Fig. 3A–C). Differences in SST responses between LGM and $2xCO_2$ persist at quasi-equilibrium in a fully coupled (atmosphere–ocean GCM) version of CESM1-CAM5 (Fig. 3C; SI Appendix, Fig. S5). Comparing the fully coupled model's response (Fig. 3C) to LGM forcing with the data-assimilation patterns (Fig. 3D) we use to quantify pattern effects suggests that LGM ice sheets amplify SST cooling in the northern extratropics (22, 28, 29) but that this pattern is more pronounced in proxy reconstructions.

Decomposing λ from our AGCM simulations into component feedbacks (SI Appendix, Fig. S6), including results from direct model output and from radiative kernels (Materials and Methods), shows that shortwave cloud feedbacks are responsible for much of the negative value of $\Delta\lambda$ and for much of the spread across AGCMs. The combined feedback from lapse rate and water vapor changes also contributes to negative values of $\Delta\lambda$, while surface albedo offsets the net difference with a positive $\Delta\lambda$. These results align with previous studies that emphasize cloud and lapse rate feedbacks in pattern effects (11, 13, 15, 20).

Spatial distributions of feedbacks (SI Appendix, Fig. S7, Text S5) clarify the connection between ice-sheet forcing, SST response, and cloud feedbacks. Where the SST cooling from LGM ice sheets is amplified in the North Pacific and North Atlantic, positive shortwave cloud feedbacks are prominent due to increases in reflective low clouds (11–15, 18, 29). Compared to $2xCO_2$ simulations, LGM reconstructions have relatively small SST anomalies in tropical ascent regions (SI Appendix, Fig. S1) where feedbacks are most negative (11–14, 18, 35). The result is that the LGM SST pattern produces a less-negative global climate feedback compared to the $2xCO_2$ SST pattern and $\Delta\lambda<0$.

Separating pattern effects from temperature dependence of feedbacks

While our explanation for feedback differences between LGM and $2xCO_2$ forcing focuses on SST pattern differences, we also estimate how $\Delta\lambda$ is affected by global-mean temperature within our AGCM simulations. We consider that

$$\Delta\lambda \approx \Delta\lambda_{PatternOnly} + \Delta\lambda_T, \quad [5]$$

where $\Delta\lambda_{PatternOnly}$ is the feedback change due to different patterns of SST anomalies and $\Delta\lambda_T$ is the feedback change due to different global-mean temperatures (T). Recent community assessments (1, 2) assume warmer climates are more sensitive ($\Delta\lambda_T>0$) (5–9, 39), which is at odds with the total $\Delta\lambda<0$ we find for the LGM in AGCMs and coupled models (Fig. 2).

To separate pattern effects from temperature dependence, we perform additional "pattern-only" simulations in CAM4, CAM5, and CAM6 using the LGMR and $2xCO_2$ patterns. For these simulations, we multiply local SST anomalies by constant scaling factors to yield global-mean

$\Delta SST=-0.5$ K with constant baseline SIC (Materials and Methods). SST scaling preserves spatial patterns of anomalies but forces global-mean ΔT to be small and equal across simulations, i.e., $\Delta\lambda_T \approx 0$ in the pattern-only simulations. We then repeat the feedback calculations, computing $\Delta\lambda_{PatternOnly}$ as in Eq. 3. We estimate the temperature dependence $\Delta\lambda_T$ as the residual difference between the main and pattern-only AGCM simulations, rearranging Eq. 5 to $\Delta\lambda_T \approx \Delta\lambda - \Delta\lambda_{PatternOnly}$ (Materials and Methods).

The magnitude and sign of $\Delta\lambda_T$ is found to be model-dependent, in agreement with recent multi-model assessments (21, 46), but $\Delta\lambda_T$ appears to be positive and directionally consistent with standard assumptions (1, 2) for feedback temperature dependence. However, $\Delta\lambda_{PatternOnly}$ is negative and larger than $\Delta\lambda_T$ such that total $\Delta\lambda<0$ in each AGCM (SI Appendix, Fig. S8, Table S3). These results suggest that total $\Delta\lambda$ for the LGM is mostly attributable to SST pattern effects, and $\Delta\lambda_T$ plays a smaller role over this range of climates. Recent assessments (1, 2) considered $\Delta\lambda_T$ for the LGM but did not account for the larger, opposing term, $\Delta\lambda_{PatternOnly}$. The substantial LGM pattern effect found here motivates revising the LGM evidence for modern-day ECS.

Climate sensitivity accounting for LGM pattern effects

Constraining modern-day ECS with paleoclimate evidence requires accounting for how forcings and feedbacks differ in paleoclimates relative to the modern-day 2xCO_2 scenario (1, 2, 5). LGM inferences of ECS begin with applying Eq. 1 to the LGM in equilibrium, estimating the unadjusted LGM feedback as $\lambda^*_{\mathrm{LGM}} = \frac{-\sum \Delta \mathrm{F}}{\Delta \mathrm{T}}$. Effective radiative forcings (ΔF) include not only CO_2 but also ice sheets (including sea level) and, depending on the timescale chosen for ECS (1–3, 5), additional changes that behave distinctly at the LGM: vegetation, dust, N_2O, and CH_4 (Materials and Methods). Finally, λ^*_{LGM} must be adjusted for differences in feedbacks ($\Delta\lambda$) relative to those operating in modern-day 2xCO_2, following Eq. 4. Note that $\Delta\lambda$ captures the impact of forcing efficacy (47), which does not need to be included separately in this framework (SI Appendix, Text S1).

To demonstrate the impact of LGM pattern effects, we follow methods in WCRP20 (1) and focus on the 150-year timescale of climate sensitivity (*S*) applicable to modern warming (1, 2) (Materials and Methods). We use WCRP20 because that assessment uniquely allows updates of individual parameters and quantitatively combines lines of evidence, but our results would have the same directional impact on other assessments (2, 3). We use forcing values from WCRP20 to estimate the unadjusted LGM feedback, λ^*_{LGM} in Eq. 4. However, given emerging evidence (2, 3, 31, 48) after WCRP20, we report results using a global temperature anomaly for the LGM of $\Delta T_{LGM}=-6\pm1$ K in addition to WCRP20's value of -5 ± 1 K. We implement our key finding by updating the LGM $\Delta\lambda$, which includes LGM pattern effects for the first time. We assign a Normal distribution to $\Delta\lambda$, $N(\mu=-0.37, \sigma=0.23)$ $Wm^{-2}K^{-1}$, reflecting spread across AGCMs and SST reconstructions (Materials and Methods). We include additional uncertainty tests in SI Appendix, Figures S4 and S9, demonstrating that our general conclusions hold if the assumed σ for $\Delta\lambda$ is doubled.

Accounting for the LGM pattern effect reduces climate sensitivity inferred from LGM evidence (Fig. 4). With $\Delta T_{LGM}\approx-6$ K, maximum likelihood for *S* from the LGM evidence alone becomes 2.0 K (change of −1.3 K). Combining the updated LGM evidence with existing likelihoods for the other lines of evidence (process understanding, historical record, and Pliocene) yields new Bayesian posterior probability distributions for the two priors in WCRP20: uniform in λ (WCRP20's "Baseline") and uniform in *S* (a robustness test).

The impact of the LGM pattern effect on the combined evidence is most pronounced on the upper bound of *S*, which has been notoriously difficult to constrain (49). Assuming $\Delta T_{LGM}\approx-6\pm1$ K, the posterior 95th percentile becomes 4.1 K (change of −0.9 K) with a uniform-λ prior or 4.7 K (change of −1.4 K) with a uniform-*S* prior. The lower bound is relatively unchanged at 2.1 K (uniform-λ) or 2.3 K (uniform-*S*). The central estimate, represented by the median *S*, becomes 2.9 K (change of −0.4 K) with a uniform-λ prior or 3.1 K (change of −0.6 K) with a uniform-*S* prior. These results place *S* in the range of 2.1–4.1°C (5–95%) for a uniform-λ prior and 2.3–4.7°C (5–95%) for a uniform-*S* prior, indicating substantially stronger constraints than WCRP20 (1) even after allowing for more glacial cooling. While the qualitative assessment in IPCC AR6 (2) cannot be quantitatively updated, these results suggest stronger constraints on modern-day ECS than assessed there, as well.

Accounting for LGM pattern effects—enabled by recent advances in LGM SST reconstruction using paleoclimate data assimilation and in quantifying pattern effects using atmospheric models—provides a tighter upper bound on modern-day ECS. While each line of evidence will surely evolve as scientific understanding improves, the results presented here demonstrate that pattern effects must be accounted for when inferring modern-day climate sensitivity from paleoclimate periods that are substantially affected by non-CO_2 forcing.

Materials and Methods

Data-assimilation reconstructions of the LGM. We use four LGM reconstructions to quantify the LGM pattern effect, sampling uncertainty (34) across data assimilation methods and model priors (50). Osman et al. (2021) produced the time-dependent Last Glacial Maximum Reanalysis ("LGMR") (31) spanning the past 24,000 years; the SST and SIC fields that represent the LGM in their reanalysis are time means spanning 19,000–23,000 years ago. Tierney et al. (2020) (3) produced the state estimate "lgmDA" dataset. Both the LGMR and lgmDA use priors from isotope-enabled simulations in iCESM1.2 and iCESM1.3 with assimilation of seasonal and annual SST proxies in an ensemble Kalman filter; there are differences in the proxy databases and methods between the two reconstructions. Annan et al. (2022) (32) also used an ensemble Kalman filter but with a multi-model prior, including 19 ensemble members from a wide array of climate models spanning PMIP2 (launched in 2002) to PMIP4 (launched in 2017); they assimilated annual SST proxies and land-temperature proxies; they also applied an adjustment to the prior ensemble to pre-center the prior around available proxy data. Amrhein et al. (2018) (33) fit the MITgcm ocean model to seasonal and annual SST proxies (51) using least-squares with Lagrange multipliers by adjusting prior atmospheric fields from a CCSM4 LGM simulation (52).

Simulations with atmospheric general circulation models. SST/SIC boundary conditions (BCs) for the LGM, Late Holocene baseline, and 2xCO_2 are prepared to maintain constant forcing, i.e., $\Delta F=0$ in Eq. 1, across simulations. Topography is held constant, i.e., the LGM ice sheets are not present in AGCM simulations because their impact is already included as a forcing, and we are isolating feedbacks from changing SST/SIC. For the LGM and Late Holocene datasets, we adjust for differences relative to modern coastlines using kriging and extrapolation in polar regions. Details of sea-level adjustments are provided in SI Appendix, Text S3.

The 2xCO_2 BC is the multi-model mean of 200 years from the end of six 2xCO_2 simulations, initialized from pre-industrial control states, in LongRunMIP (37): CESM1.0.4 (years 2300-2500), CNRM-CM6-1 (years 550-750), HadCM3L (years 500-700), MPI-ESM-1.2 (years 800-1000), GFDL-ESM2M (years 4300-4500), and MIROC3.2 (years 1803-2003). These simulations are near equilibrium but only represent an estimate of the true equilibrium SST response to 2xCO_2.

The Late Holocene, defined as the climatological mean of 0–4,000 years ago in the LGMR (31), is used as the baseline SST/SIC for all feedback calculations. This baseline represents a long-term mean of the pre-industrial climate, constrained by assimilation of proxy data. After adjusting for modern sea level, the four LGM BCs and the 2xCO_2 BC for SST are prepared by adding the SST anomalies from each of the four reconstructions to the Late Holocene baseline SST. Due to nonlinear behavior of sea ice, the LGM and 2xCO_2 BCs for SIC are not added to the baseline as anomalies but rather are used directly (SI Appendix, Fig. S2).

We run simulations with the Late Holocene baseline, 2xCO_2, and LGMR in each of five AGCMs. We run simulations with all four of the LGM reconstructions (LGMR, lgmDA, Amrhein, Annan) in CAM4 and CAM5, sampling the spread in LGM feedbacks from different reconstructions in two AGCMs with distinct relationships linking SST patterns to radiative feedbacks based on Green's functions (12, 18). Spin-up/analysis period/climatological forcing for each AGCM is 5yr/25yr/2000 (CESM1.2.2.1-CAM4 (53), CESM1.2.2.1-CAM5 (54), and CESM2.1-CAM6 (55) at 1.9°x2.5° latitude-by-longitude resolution); 5yr/25yr/2014 (HadGEM3-GC3.1-LL (56) at N96, ~135-km resolution) and 1yr/30yr/2001 (GFDL-AM4 (57) at C96, ~100-km resolution). Parent coupled models of the AGCMs considered here sample a wide range of climate sensitivities, from 2.95 K to 5.54 K, and the AGCMs span a wide range of pattern effects in the historical record, from 0.38 $Wm^{-2}K^{-1}$ to 0.84 $Wm^{-2}K^{-1}$ (17).

To compute λ, we take global means over the analysis periods for net top-of-atmosphere radiative imbalance (N) and near-surface air temperature (T). Differences are taken relative to the Late Holocene baseline, yielding "effective" feedbacks (58) as λ=ΔN/ΔT for LGM and $2xCO_2$ simulations, given that ΔF=0 in Eq. 1 by design.

To evaluate the impact of uncertainty in the $2xCO_2$ pattern, we also consider existing simulations of abrupt-$4xCO_2$ with 150-yr regressions (59) of ΔN versus ΔT, denoted as $\lambda_{4x(150yr)}$, to estimate λ_{2x} (results in SI Appendix, Figs. S3–S4, Tables S1–S2). Results are consistent using either method of estimating λ_{2x}. To compute Δλ using $\lambda_{4x(150yr)}$, we apply a timescale adjustment (ζ) to reconcile feedbacks from equilibrium paleoclimate data with the feedback that applies to 150-year "effective" sensitivity (*S*), as in WCRP20. We use the central estimate from WCRP20 of ζ=0.06, and Eq. 3 is modified to $\Delta\lambda=\lambda_{4x(150yr)}/(1+\zeta)-\lambda_{LGM}$.

To investigate how spread across the ensemble members from the two most recent LGM reconstructions affects our results, we run additional simulations using CAM4 and CAM5 with the quartiles of ensemble members that produce the most-negative and most-positive λ_{LGM} in the LGMR (31) and Annan (32) reconstructions (error bars in Fig. 2). To determine the SST/SIC boundary conditions for these experiments, ensemble members in each dataset are initially ranked by estimating λ_{LGM} with CAM5 Green's functions (18) applied to SST anomalies from each ensemble member. CAM4 Green's functions (12) produce similar rankings. Green's functions are only used for ranking and discarded thereafter. We group the ensemble members into quartiles based on rank, and the mean SST/SIC (only SST for the Annan reconstruction) is computed across ensemble members in each quartile. Mean SST anomalies representing the 1st and 4th quartiles, the most- and least-negative feedbacks, are used in the additional AGCM simulations. Note that CAM5 with the Annan ensemble's extreme-negative λ_{LGM} produces Δλ>0. In this quartile, most ensemble members have warming at the LGM over substantial portions of the Southern Ocean (SI Appendix, Fig. S10). This suggests that Δλ could be positive if the Southern Ocean experienced warming at the LGM, which appears unlikely based on SST proxies (3, 31, 60), reconstructed deep-ocean temperatures (61), and proxy data indicating increased Antarctic sea ice at the LGM (62).

Pattern-only simulations separating pattern and temperature dependence. Feedback differences can be attributed to differences in SST patterns and in global-mean near-surface air temperature (1), such that $\Delta\lambda\approx\Delta\lambda_{PatternOnly}+\Delta\lambda_T$. To separate pattern and temperature impacts on Δλ, we conduct additional "pattern-only" simulations in CAM4, CAM5, and CAM6 with the LGMR and $2xCO_2$ patterns. For these simulations, we multiply local SST anomalies by constant scale factors, *k*, which are determined for each pattern so that the global-mean ΔSST is reduced to −0.5 K for both simulations. The constant scale factor for a given pattern of anomalies is calculated from the global-mean ΔSST as $k=\frac{-0.5\ K}{\overline{\Delta SST}_{global}}$, and scaled patterns are then created as $\Delta SST_{scaled}=k\Delta SST$ at each gridcell. We hold SIC constant at the Late Holocene baseline.

SST scaling preserves the spatial pattern of anomalies but forces global-mean ΔT to be small enough that feedback changes due to temperature dependence are negligible ($\Delta\lambda_T\approx0$). We repeat the feedback calculations, computing $\Delta\lambda_{PatternOnly}\approx\lambda_{2x}^{-0.5\mathrm{K}}-\lambda_{\mathrm{LGM}}^{-0.5\mathrm{K}}$ as in Eq. 3. While there is no existing method that directly isolates temperature dependence in AGCM simulations, the temperature dependence can be approximated as the residual difference between our main and pattern-only simulations, rearranging Eq. 5 to $\Delta\lambda_T\approx\Delta\lambda-\Delta\lambda_{PatternOnly}$. In this framework, feedback changes due to sea ice are included in temperature dependence.

We employ this pattern-scaling method because it aligns with intuition for pattern effects captured by Green's functions (12, 18). We do not use Green's functions to calculate the pattern-only feedbacks, but we briefly discuss the Green's functions framework here to explain the pattern-only AGCM simulations. In the linear framework of Green's functions,

$$\Delta N=\sum_j \frac{\partial N}{\partial SST_j}\Delta SST_j+\epsilon_N,$$

$$\Delta T=\sum_j \frac{\partial T}{\partial SST_j}\Delta SST_j + \epsilon_T,$$

where j represents each gridcell, ΔSST_j represents the full SST anomaly at gridcell j, $\partial N/\partial SST_j$ represents the global-mean top-of-atmosphere radiative response to a unit increase in local SST at gridcell j, $\partial T/\partial SST_j$ similarly represents the response of global-mean near-surface air temperature, and ϵ represents changes that are independent of SST. Because the feedback $\lambda=\Delta N/\Delta T$, constant scale factors, applied as $k\Delta SST$, appear in the feedback calculation as $\lambda=(k\Delta N)/(k\Delta T)$ if $\epsilon_N=\epsilon_T=0$ and SST patterns determine λ. In this case where SST patterns are the sole control on λ, scale factors cancel and have no effect on feedbacks or pattern effects. By comparing feedbacks from scaled pattern-only simulations with feedbacks from simulations with full SST anomalies, we quantify feedback changes that cannot be explained by SST patterns, which we attribute to feedback dependence on global-mean temperature. For example, temperature dependence could arise from $\frac{\partial N}{\partial SST_j}$ changing with global-mean temperature or from sea ice appearing at lower latitudes as temperature decreases.

Feedback decomposition using model fields and radiative kernels. Net λ is calculated from changes in top-of-atmosphere radiation (ΔN) divided by changes in global-mean temperature (ΔT). ΔN can be separated into shortwave clear-sky (SWcs), longwave clear-sky (LWcs), and cloud radiative effect (CRE):

$$\Delta N=\Delta N_{SWcs}+\Delta N_{LWcs}+\Delta N_{CRE}.$$

Each component of the radiation is available from AGCM output, and dividing all terms by ΔT yields feedbacks for each component which sum to the net feedback. The total clear-sky feedback is the sum of shortwave and longwave components. Because CRE is calculated as all-sky radiation (N) minus clear-sky radiation, CRE is affected by changes in non-cloud variables.

With radiative kernels (63, 64), feedbacks can be decomposed into contributions from temperature, moisture, and surface albedo. Cloud feedbacks can be estimated by controlling for changes in non-cloud variables, which we do here following past studies (64). Radiative kernels are linearized around a specific climate in a specific model, however, and are prone to errors when applied to different climates and models. We use CAM5 kernels (65), convolving them with the monthly mean climatology of anomalies in each AGCM simulation to produce feedbacks in SI Appendix, Figures S6–S7, and zonal means in Figures S12–S22. HadGEM3-GC3.1-LL is not included in kernel analysis due to model-output limitations. GFDL-AM4's 2xCO_2 simulation has error in the kernel-derived clear-sky feedback equal to 15.6% of the actual feedback, exceeding the 15% threshold commonly used as a test of clear-sky linearity (15, 63); all other simulations have clear-sky feedback errors less than 10%. Residuals shown in SI Appendix, Figure S6, are based on total (all-sky) radiation: $\lambda_{Residual}=\lambda_{Net}-\Sigma\lambda_j$, where λ_{Net} is the net feedback from model output, and $\Sigma\lambda_j$ is the sum of each of the following kernel-derived feedbacks: Planck, lapse rate, water vapor, surface albedo, shortwave cloud, and longwave cloud.

Bayesian estimate of modern-day climate sensitivity. We follow methods (1) and code (66) provided by WCRP20 for calculating climate sensitivity, but we provide a summary of relevant methods here. Equilibrium climate sensitivity (ECS) is the steady-state change in global-mean temperature (T) from a doubling of CO_2, traditionally with ice sheets and vegetation assumed fixed. When inferring climate sensitivity that is relevant to modern warming from paleoclimate evidence, changes in the paleoclimate radiative budget that are distinct from feedback processes in modern-day 2xCO_2 are treated as forcings; this is typically accomplished by separating 'slow' timescale changes as forcings (e.g., ice sheets) from 'fast' timescale changes as feedbacks (5). WCRP20 applies this framework by focusing on "effective" climate sensitivity (S), i.e., the 150-year system response.

Relative to WCRP20, our key update only affects Δλ for the LGM. However, given evidence (2, 3, 31, 48) published after WCRP20 showing LGM cooling centered around −6ºC instead of −5ºC, we report our main results using both assumptions for ΔT_{LGM} (Fig. 4; SI Appendix, Fig. S4).

To estimate S, we use a modified version of WCRP20's energy balance for the LGM,

$$\Delta T_{LGM} = \frac{-(-0.57\Delta F_{2x}+\Delta F')}{\frac{\lambda_{2x}}{1+\zeta}-\Delta\lambda}, \quad [6]$$

which determines λ_{2x} and $S=-\Delta F_{2x}/\lambda_{2x}$. We substitute our $\Delta\lambda$, which includes pattern and temperature dependence. Other than testing a colder ΔT_{LGM}, the parameters are unchanged from WCRP20 with the following Normal distributions: modern-day forcing from $2xCO_2$ ΔF_{2x}~$N(\mu=4.0, \sigma=0.3)$ Wm^{-2}; total non-CO_2 LGM forcing of $\Delta F'$~$N(-6.15, 2)$ Wm^{-2} (consisting of −3.2 Wm^{-2} from ice sheets, −1.1 from vegetation, −1.0 from dust aerosols, −0.28 from N_2O, and −0.57 from CH_4); the timescale transfer parameter from ECS to the 150-year feedback of ζ~$N(0.06, 0.2)$; and LGM temperature change ΔT_{LGM}~$N(-5, 1)$ ºC, or revised ΔT_{LGM}~$N(-6, 1)$ ºC. In WCRP20, $\Delta\lambda=\Delta\lambda_T=-\alpha\Delta T_{LGM}/2$, with α~$N(\mu=0.1, \sigma=0.1)$ $Wm^{-2}K^{-2}$.

Quantification of non-CO_2 effective radiative forcing from ice sheets (including sea level), dust aerosols, vegetation, and other greenhouse gases represents substantial uncertainty. As noted in ref. (22), estimates of the effective radiative forcing for each component of LGM forcing still need to be constrained. Recent assessments (1–3) discuss how dust aerosols (67, 68), vegetation, and non-CO_2 greenhouse gases also act as feedbacks on fast timescales, hence ref. (3) shows multiple options for calculating LGM sensitivity. IPCC AR6 (2) presents these non-CO_2 changes as feedbacks (central value of −0.01 $Wm^{-2}K^{-1}$) in their framework for modern-day ECS, but AR6 does not address how to account for the LGM's distinct non-CO_2 changes (other than ice sheets) when estimating modern-day ECS from LGM evidence.

From the AGCM results in this study, we incorporate pattern effects in $\Delta\lambda$ of Eq. 6, assigning a revised $\Delta\lambda$~$N(-0.37, 0.23)$ $Wm^{-2}K^{-1}$. The revised distribution for $\Delta\lambda$ in our study is based on propagating uncertainty, estimated as spread across AGCMs and LGM reconstructions. To combine uncertainty, we assume that within CAM6, GFDL-AM4, and HadGEM3, the spread in $\Delta\lambda$ from different LGM reconstructions would be the same as in CAM4 and CAM5. We add the differences in $\Delta\lambda$ from each pattern in CAM4 and CAM5, where differences are computed relative to $\Delta\lambda$ using the LGMR pattern, to the results from the remaining three AGCMs. The effect is to treat errors as arising independently in reconstructions and AGCMs. We include $\Delta\lambda$ from extreme-quartile simulations using ensemble members from Annan and LGMR as part of the combined sample. There are 8 simulations from CAM4 and 8 from CAM5 that determine spread from LGM patterns. Note that the spread from LGM patterns is similar between CAM4 and CAM5 (Fig. 2).

With the combined sample, we perform bootstrap resampling (described in SI Appendix, Text S4) with 10^5 iterations and a sample size of 19 (equal to the number of actual AGCM simulations). The mean over all iterations is $\overline{\Delta\lambda}=-0.37$ (95% range: −0.47 to −0.26) $Wm^{-2}K^{-1}$, and mean sample standard deviation = 0.23 (95% range: 0.15 to 0.31) $Wm^{-2}K^{-1}$, which informs our assigned μ and σ, respectively. In SI Appendix, Figure S4, we include an uncertainty test by doubling σ to 0.46 $Wm^{-2}K^{-1}$.

Calculations for LGM likelihoods and Bayesian probability density functions (PDF) for *S* follow the Monte Carlo methods in WCRP20 (1, 66). Likelihoods are independent of the prior, but combining the likelihoods with a prior is required to create posterior PDFs that combine lines of evidence. We show results for both priors in WCRP20: the Uniform(−10, 10) $Wm^{-2}K^{-1}$ prior on λ (their "Baseline") and the Uniform(0, 20) ºC prior on S (robustness test, using a prior that is more conservative regarding the possibility of high climate sensitivity).

Data, Materials, and Software Availability

SST/SIC boundary conditions and AGCM results are available in a Github repository at github.com/vtcooper/cooper_etal_2023_LGMpattern. LongRunMIP is available at longrunmip.org, LGMR (31) at doi.org/10.25921/njxd-hg08, lgmDA(3) v2.1 at doi.org/10.5281/zenodo.5171432, Amrhein (33) at doi.org/10.5281/zenodo.8110710, and Annan (32) at doi.org/10.5194/cp-18-1883-2022. Previous studies' coupled-model output is hosted at doi.org/10.5281/zenodo.3948405 (CESM1-CAM5) (22), doi.org/10.5281/zenodo.4075596 (CESM2-CAM6) (44), and doi.org/10.5065/bdr7-wt42 (CESM2-PaleoCalibr) (45). Code from WCRP20 to calculate climate sensitivity is available at doi.org/10.5281/zenodo.3945276 (66). CAM5 radiative kernels (65) are available through doi.org/10.5281/zenodo.997899.

Acknowledgments

V.T.C. acknowledges funding from the NDSEG Fellowship (USA Dept. of Defense) and NCAR/CISL/Cheyenne computing (doi:10.5065/D6RX99HX). V.T.C., K.C.A., and G.J.H. acknowledge funding from National Science Foundation (NSF) Award OCE-2002276; J.E.T. and M.B.O. from NSF OCE-2002398; C.P. from NSF OCE-2002385; N.J.B. from NSF OCE-2002448 and AGS-1844380. K.C.A. acknowledges funding from the National Oceanic and Atmospheric Administration (NOAA) MAPP Program Award NA20OAR4310391 and an Alfred P. Sloan Research Fellowship (Grant FG-2020-13568). Y.D. was supported by the NOAA Climate and Global Change Postdoctoral Fellowship Program, administered by UCAR's Cooperative Programs for the Advancement of Earth System Science (CPAESS) under award NA210AR4310383. T.A. was supported by the Met Office Hadley Centre Climate Programme funded by BEIS and received funding from the European Union's Horizon 2020 research and innovation programme under grant agreement 820829. The CESM project is supported primarily by the NSF. This material is based upon work supported by the National Center for Atmospheric Research, which is a major facility sponsored by the NSF under Cooperative Agreement No. 1852977.

References

1. S. C. Sherwood, *et al.*, An Assessment of Earth's Climate Sensitivity Using Multiple Lines of Evidence. *Reviews of Geophysics* **58** (2020).
2. P. Forster, *et al.*, "2021: The Earth's energy budget, climate feedbacks, and climate sensitivity" in *Climate Change 2021: The Physical Science Basis. Contribution of Working Group I to the Sixth Assessment Report of the Intergovernmental Panel on Climate Change*, V. Masson-Delmotte, *et al.*, Eds. (Cambridge Univ. Press, 2021) https:/doi.org/10.1017/9781009157896.009.
3. J. E. Tierney, *et al.*, Glacial cooling and climate sensitivity revisited. *Nature* **584**, 569–573 (2020).
4. S. Manabe, K. Bryan, CO_2 -induced change in a coupled ocean-atmosphere model and its paleoclimatic implications. *J Geophys Res* **90**, 11689 (1985).
5. PALAEOSENS Project Members, Making sense of palaeoclimate sensitivity. *Nature* **491**, 683–691 (2012).
6. P. Köhler, B. de Boer, A. S. von der Heydt, L. B. Stap, R. S. W. van de Wal, On the state dependency of the equilibrium climate sensitivity during the last 5 million years. *Climate of the Past* **11**, 1801–1823 (2015).
7. A. S. von der Heydt, *et al.*, Lessons on Climate Sensitivity From Past Climate Changes. *Curr Clim Change Rep* **2**, 148–158 (2016).
8. T. Friedrich, A. Timmermann, M. Tigchelaar, O. E. Timm, A. Ganopolski, Nonlinear climate sensitivity and its implications for future greenhouse warming. *Sci Adv* **2** (2016).
9. E. J. Rohling, *et al.*, Comparing Climate Sensitivity, Past and Present. *Ann Rev Mar Sci* **10**, 261–288 (2018).
10. K. C. Armour, C. M. Bitz, G. H. Roe, Time-Varying Climate Sensitivity from Regional Feedbacks. *J Clim* **26**, 4518–4534 (2013).
11. C. Zhou, M. D. Zelinka, S. A. Klein, Impact of decadal cloud variations on the Earth's energy budget. *Nat Geosci* **9**, 871–874 (2016).
12. Y. Dong, C. Proistosescu, K. C. Armour, D. S. Battisti, Attributing Historical and Future Evolution of Radiative Feedbacks to Regional Warming Patterns using a Green's Function Approach: The preeminence of the Western Pacific. *J Clim* (2019) https:/doi.org/10.1175/JCLI-D-18-0843.1.
13. T. Andrews, M. J. Webb, The Dependence of Global Cloud and Lapse Rate Feedbacks on the Spatial Structure of Tropical Pacific Warming. *J Clim* **31**, 641–654 (2018).

14. S. Fueglistaler, Observational Evidence for Two Modes of Coupling Between Sea Surface Temperatures, Tropospheric Temperature Profile, and Shortwave Cloud Radiative Effect in the Tropics. *Geophys Res Lett* **46**, 9890–9898 (2019).
15. P. Ceppi, J. M. Gregory, Relationship of tropospheric stability to climate sensitivity and Earth's observed radiation budget. *Proceedings of the National Academy of Sciences* **114**, 13126–13131 (2017).
16. T. Andrews, *et al.*, Accounting for Changing Temperature Patterns Increases Historical Estimates of Climate Sensitivity. *Geophys Res Lett* **45**, 8490–8499 (2018).
17. T. Andrews, *et al.*, On the Effect of Historical SST Patterns on Radiative Feedback. *Journal of Geophysical Research: Atmospheres* **127** (2022).
18. C. Zhou, M. D. Zelinka, S. A. Klein, Analyzing the dependence of global cloud feedback on the spatial pattern of sea surface temperature change with a Green's function approach. *J Adv Model Earth Syst* **9**, 2174–2189 (2017).
19. K. C. Armour, J. Marshall, J. R. Scott, A. Donohoe, E. R. Newsom, Southern Ocean warming delayed by circumpolar upwelling and equatorward transport. *Nat Geosci* **9**, 549–554 (2016).
20. Y. Dong, *et al.*, Intermodel Spread in the Pattern Effect and Its Contribution to Climate Sensitivity in CMIP5 and CMIP6 Models. *J Clim* **33**, 7755–7775 (2020).
21. M. Renoult, N. Sagoo, J. Zhu, T. Mauritsen, Causes of the weak emergent constraint on climate sensitivity at the Last Glacial Maximum. *Climate of the Past* **19**, 323–356 (2023).
22. J. Zhu, C. J. Poulsen, Last Glacial Maximum (LGM) climate forcing and ocean dynamical feedback and their implications for estimating climate sensitivity. *Climate of the Past* **17**, 253–267 (2021).
23. P. Braconnot, M. Kageyama, Shortwave forcing and feedbacks in Last Glacial Maximum and Mid-Holocene PMIP3 simulations. *Philosophical Transactions of the Royal Society A: Mathematical, Physical and Engineering Sciences* **373**, 20140424 (2015).
24. S. Manabe, A. J. Broccoli, The influence of continental ice sheets on the climate of an ice age. *J Geophys Res* **90**, 2167 (1985).
25. K. H. Cook, I. M. Held, Stationary Waves of the Ice Age Climate. *J Clim* **1**, 807–819 (1988).
26. S.-Y. Lee, J. C. H. Chiang, P. Chang, Tropical Pacific response to continental ice sheet topography. *Clim Dyn* **44**, 2429–2446 (2015).
27. P. N. DiNezio, *et al.*, Glacial changes in tropical climate amplified by the Indian Ocean. *Sci Adv* **4** (2018).
28. W. H. G. Roberts, C. Li, P. J. Valdes, The Mechanisms that Determine the Response of the Northern Hemisphere's Stationary Waves to North American Ice Sheets. *J Clim* **32**, 3917–3940 (2019).
29. D. J. Amaya, *et al.*, Air-sea coupling shapes North American hydroclimate response to ice sheets during the Last Glacial Maximum. *Earth Planet Sci Lett* **578** (2022).
30. G. J. Hakim, *et al.*, The last millennium climate reanalysis project: Framework and first results. *Journal of Geophysical Research: Atmospheres* **121**, 6745–6764 (2016).
31. M. B. Osman, *et al.*, Globally resolved surface temperatures since the Last Glacial Maximum. *Nature* **599**, 239–244 (2021).
32. J. D. Annan, J. C. Hargreaves, T. Mauritsen, A new global surface temperature reconstruction for the Last Glacial Maximum. *Climate of the Past* **18**, 1883–1896 (2022).
33. D. E. Amrhein, C. Wunsch, O. Marchal, G. Forget, A Global Glacial Ocean State Estimate Constrained by Upper-Ocean Temperature Proxies. *J Clim* **31**, 8059–8079 (2018).
34. D. E. Amrhein, G. J. Hakim, L. A. Parsons, Quantifying Structural Uncertainty in Paleoclimate Data Assimilation With an Application to the Last Millennium. *Geophys Res Lett* **47** (2020).
35. S. M. Kang, S. P. Xie, Dependence of Climate Response on Meridional Structure of External Thermal Forcing. *J Clim* **27**, 5593–5600 (2014).
36. B. E. J. Rose, *et al.*, The dependence of transient climate sensitivity and radiative feedbacks on the spatial pattern of ocean heat uptake. *Geophys Res Lett* **41**, 1071–1078 (2014).

37. M. Rugenstein, *et al.*, LongRunMIP: Motivation and Design for a Large Collection of Millennial-Length AOGCM Simulations. *Bull Am Meteorol Soc* **100**, 2551–2570 (2019).
38. M. Crucifix, Does the Last Glacial Maximum constrain climate sensitivity? *Geophys Res Lett* **33**, L18701 (2006).
39. M. Yoshimori, J. C. Hargreaves, J. D. Annan, T. Yokohata, A. Abe-Ouchi, Dependency of Feedbacks on Forcing and Climate State in Physics Parameter Ensembles. *J Clim* **24**, 6440–6455 (2011).
40. L. B. Stap, P. Köhler, G. Lohmann, Including the efficacy of land ice changes in deriving climate sensitivity from paleodata. *Earth System Dynamics* **10**, 333–345 (2019).
41. J. D. Shakun, Modest global-scale cooling despite extensive early Pleistocene ice sheets. *Quat Sci Rev* **165**, 25–30 (2017).
42. P. O. Hopcroft, P. J. Valdes, How well do simulated last glacial maximum tropical temperatures constrain equilibrium climate sensitivity? *Geophys Res Lett* **42**, 5533–5539 (2015).
43. C. M. Bitz, *et al.*, Climate Sensitivity of the Community Climate System Model, Version 4. *J Clim* **25**, 3053–3070 (2012).
44. J. Zhu, *et al.*, Assessment of Equilibrium Climate Sensitivity of the Community Earth System Model Version 2 Through Simulation of the Last Glacial Maximum. *Geophys Res Lett* **48** (2021).
45. J. Zhu, *et al.*, LGM Paleoclimate Constraints Inform Cloud Parameterizations and Equilibrium Climate Sensitivity in CESM2. *J Adv Model Earth Syst* **14**, e2021MS002776 (2022).
46. J. Bloch-Johnson, *et al.*, Climate Sensitivity Increases Under Higher CO_2 Levels Due to Feedback Temperature Dependence. *Geophys Res Lett* **48**, e2020GL089074 (2021).
47. C. Zhou, *et al.*, Explaining Forcing Efficacy With Pattern Effect and State Dependence. *Geophys Res Lett* **50** (2023).
48. A. M. Seltzer, *et al.*, Widespread six degrees Celsius cooling on land during the Last Glacial Maximum. *Nature* **593**, 228–232 (2021).
49. R. Knutti, G. C. Hegerl, The equilibrium sensitivity of the Earth's temperature to radiation changes. *Nat Geosci* **1**, 735–743 (2008).
50. L. A. Parsons, *et al.*, Do Multi-Model Ensembles Improve Reconstruction Skill in Paleoclimate Data Assimilation? *Earth and Space Science* **8**, e2020EA001467 (2021).
51. C. Waelbroeck, *et al.*, Constraints on the magnitude and patterns of ocean cooling at the Last Glacial Maximum. *Nature Geoscience 2009 2:2* **2**, 127–132 (2009).
52. E. C. Brady, B. L. Otto-Bliesner, J. E. Kay, N. Rosenbloom, Sensitivity to Glacial Forcing in the CCSM4. *J Clim* **26**, 1901–1925 (2013).
53. R. B. Neale, *et al.*, The Mean Climate of the Community Atmosphere Model (CAM4) in Forced SST and Fully Coupled Experiments. *J Clim* **26**, 5150–5168 (2013).
54. R. B. Neale, *et al.*, "Description of the NCAR Community Atmosphere Model (CAM 5.0) (NCAR/TN-486+STR)" (2012) https:/doi.org/http://dx.doi.org/10.5065/wgtk-4g06.
55. G. Danabasoglu, *et al.*, The Community Earth System Model Version 2 (CESM2). *J Adv Model Earth Syst* **12** (2020).
56. K. D. Williams, *et al.*, The Met Office Global Coupled Model 3.0 and 3.1 (GC3.0 and GC3.1) Configurations. *J Adv Model Earth Syst* **10**, 357–380 (2017).
57. I. M. Held, *et al.*, Structure and Performance of GFDL's CM4.0 Climate Model. *J Adv Model Earth Syst* **11**, 3691–3727 (2019).
58. M. A. A. Rugenstein, K. C. Armour, Three Flavors of Radiative Feedbacks and Their Implications for Estimating Equilibrium Climate Sensitivity. *Geophys Res Lett* **48** (2021).
59. J. M. Gregory, A new method for diagnosing radiative forcing and climate sensitivity. *Geophys Res Lett* **31**, L03205 (2004).
60. C. Waelbroeck, *et al.*, Constraints on the magnitude and patterns of ocean cooling at the Last Glacial Maximum. *Nature Geoscience 2009 2:2* **2**, 127–132 (2009).
61. J. F. Adkins, K. McIntyre, D. P. Schrag, The Salinity, Temperature, and $\delta^{18}O$ of the Glacial Deep Ocean. *Science (1979)* **298**, 1769–1773 (2002).

62. R. A. Green, *et al.*, Evaluating seasonal sea-ice cover over the Southern Ocean at the Last Glacial Maximum. *Climate of the Past* **18**, 845–862 (2022).
63. K. M. Shell, J. T. Kiehl, C. A. Shields, Using the Radiative Kernel Technique to Calculate Climate Feedbacks in NCAR's Community Atmospheric Model. *J Clim* **21**, 2269–2282 (2008).
64. B. J. Soden, *et al.*, Quantifying Climate Feedbacks Using Radiative Kernels. *J Clim* **21**, 3504–3520 (2008).
65. A. G. Pendergrass, "CAM5 Radiative Kernels [Data set]" (2017) https:/doi.org/doi.org/10.5065/D6F47MT6.
66. M. Webb, "Code and Data for WCRP Climate Sensitivity Assessment" (2020) https:/doi.org/10.5281/zenodo.3945275.
67. N. Sagoo, T. Storelvmo, Testing the sensitivity of past climates to the indirect effects of dust. *Geophys Res Lett* **44**, 5807–5817 (2017).
68. S. Albani, *et al.*, Aerosol-Climate Interactions During the Last Glacial Maximum. *Curr Clim Change Rep* **4**, 99–114 (2018).
69. J. Zhu, C. J. Poulsen, J. E. Tierney, Simulation of Eocene extreme warmth and high climate sensitivity through cloud feedbacks. *Sci Adv* **5** (2019).

Figures and Tables

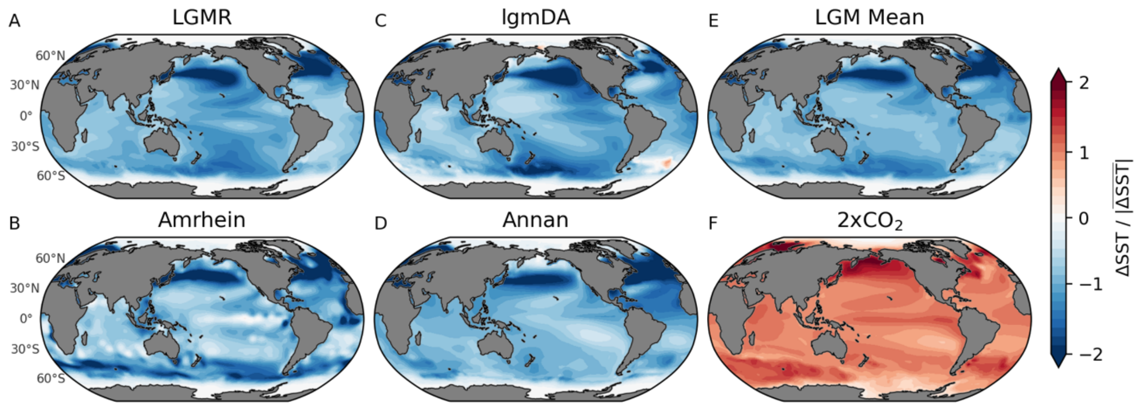

Figure 1. Patterns of sea-surface-temperature (SST) anomalies from data assimilation at the Last Glacial Maximum (LGM) compared to modern-day doubling of CO_2 (2xCO_2). LGM reconstructions include (A) Last Glacial Maximum Reanalysis (LGMR) (31), (B) Amrhein (33), (C) lgmDA (3), (D) Annan (32), and (E) the mean of the four LGM patterns. (F) Pattern of the multi-model mean from near-equilibrium simulations in LongRunMIP (37) of 2xCO_2, initialized from pre-industrial control. To show SST patterns, local SST anomalies are divided by absolute values of global-mean SST anomalies (consistent with feedbacks being radiative responses divided by temperature anomalies). All panels show annual means. LGM reconstructions are infilled to modern coastlines (Materials and Methods).

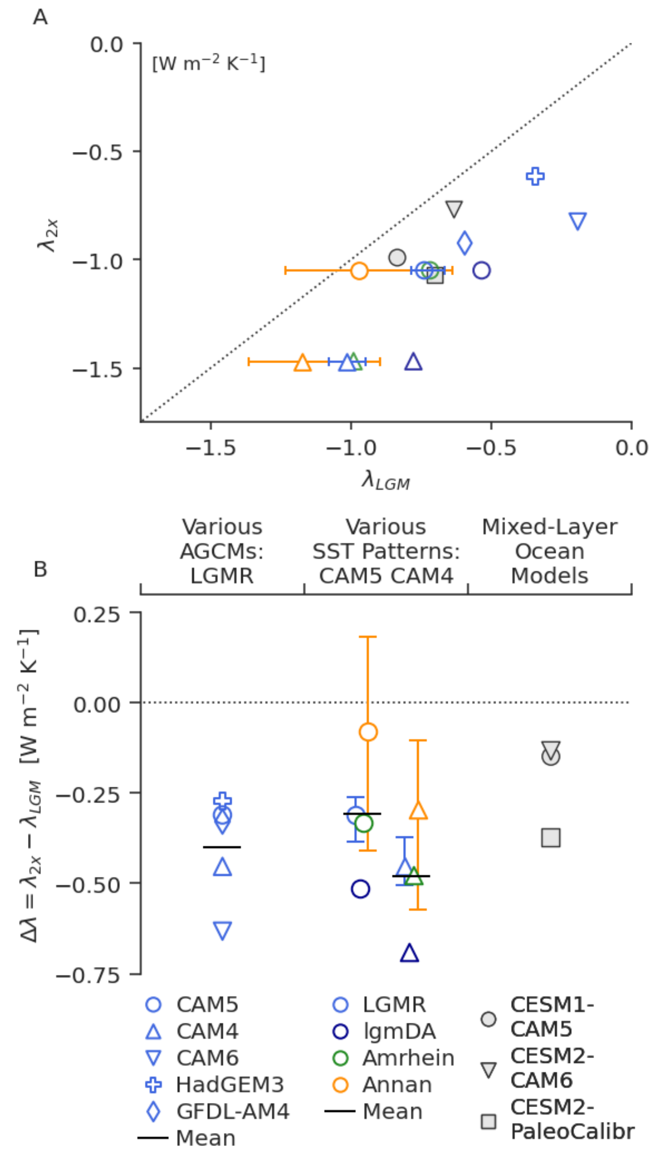

Figure 2. Last Glacial Maximum (LGM) and 2xCO_2 climate feedbacks and LGM pattern effect ($\Delta\lambda$). Different atmospheric general circulation models (AGCMs), all using the LGMR pattern for the LGM, are indicated by symbols; different LGM patterns (in CAM5 and CAM4) are indicated by colors. Error bars for Annan and LGMR represent 1st and 4th quartiles of ensemble members (Materials and Methods); central values indicate ensemble mean. For comparison with AGCM results using LGM data assimilation, the following feedbacks (in mixed-layer ocean coupled to AGCM) from previous studies are also included: CESM1-CAM5 (22), CESM2-CAM6 (44), and CESM2-PaleoCalibr (45) (modified version of CAM6). (A) Scatter plot of 2xCO_2 feedbacks, λ_{2x}, versus LGM feedbacks, λ_{LGM}, with $\lambda_{2x}=\lambda_{LGM}$ shown as dotted line. (B) LGM pattern effect, $\Delta\lambda=\lambda_{2x}-\lambda_{LGM}$, using feedbacks shown in panel A, with $\Delta\lambda=0$ shown as dotted line.

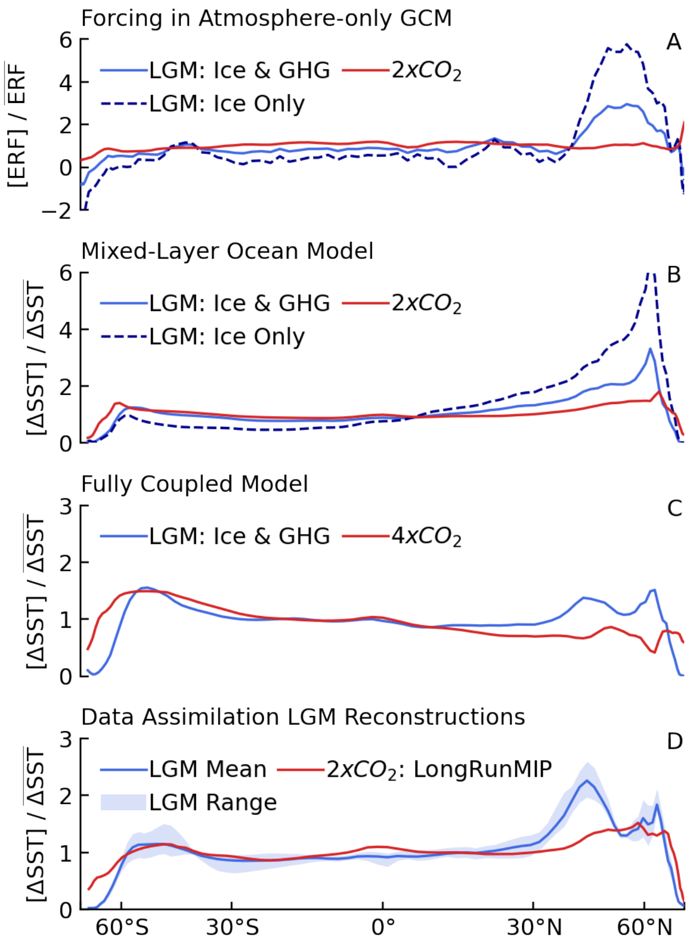

Figure 3. Zonal-mean patterns of effective radiative forcing (ERF) and sea-surface-temperature (SST) anomalies. All anomalies are normalized through division by global-mean anomalies. (A–C) Model simulations in CESM1-CAM5 from Zhu & Poulsen (22). (A) ERF directly from three fixed-SST simulations using atmospheric general circulation model with LGM greenhouse-gas (GHG) and ice-sheet (Ice) forcing, $2xCO_2$, and LGM ice-sheet forcing alone (22) (including coastline changes). (B) Equilibrium SST patterns (corresponding to panel A) in coupled mixed-layer ocean model. (C) Quasi-equilibrium SST patterns from fully coupled atmosphere-ocean model, comparing LGM forcings (22) with abrupt-$4xCO_2$ forcing (69); no long-run $2xCO_2$ simulation is available. Note vertical-axis scales. (D) Mean and range of SST patterns from four data-assimilation reconstructions (3, 31–33) of the LGM compared to $2xCO_2$ multi-model mean from LongRunMIP (37), which includes six near-equilibrium simulations of 700–4500 years.

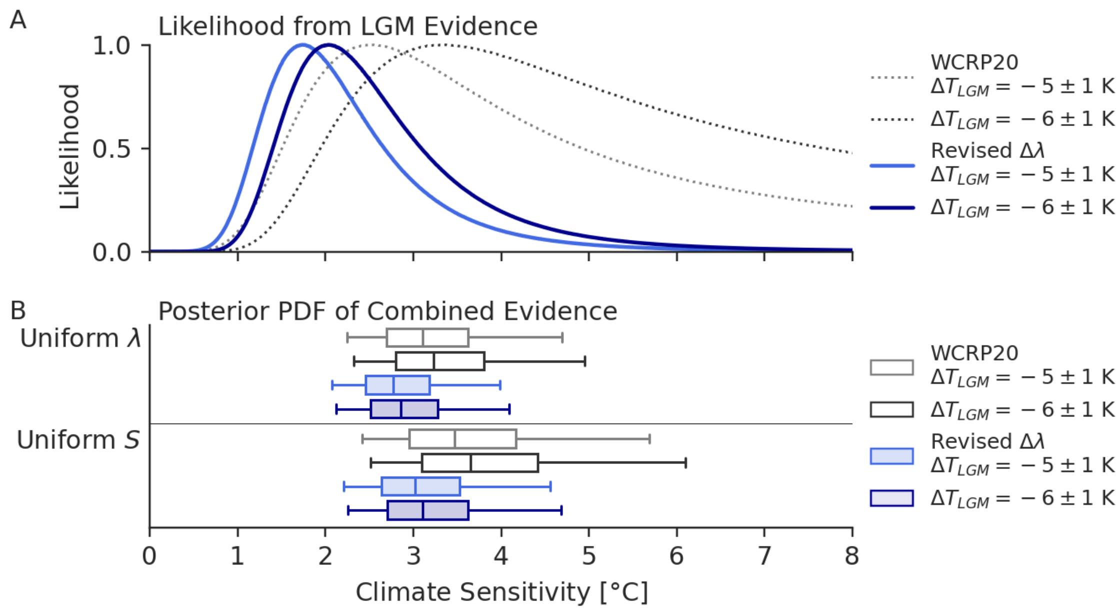

Figure 4. Inference of modern-day climate sensitivity including the LGM pattern effect. Results from WCRP20 (1) with no LGM pattern effects and original assumption of $\Delta T_{LGM} \sim N(\mu=-5, \sigma=1)$ °C (gray) and with revised $\Delta T_{LGM} \sim N(-6, 1)$ °C (black) based on IPCC AR6 (2). Revised climate sensitivity including LGM pattern effects from this study (light and dark blue) assuming $\Delta\lambda \sim N(\mu=-0.37, \sigma=0.23)$ $Wm^{-2}K^{-1}$. Climate sensitivity shown is effective sensitivity (S) representing 150-year response, as in WCRP20 (1). (A) Likelihood functions for S based on only the LGM line of evidence. (B) Posterior PDF after combining LGM with other lines of evidence, assuming a uniform-λ prior (upper panel) or a uniform-S prior (lower panel). Outlier lines indicate 5–95th percentiles while box indicates 25–75th percentiles and median.

Supporting Information for

Last Glacial Maximum pattern effects reduce climate sensitivity estimates.

Vincent T. Cooper[a,*], Kyle C. Armour[a,b], Gregory J. Hakim[a], Jessica E. Tierney[c], Matthew B. Osman[d], Cristian Proistosescu[e], Yue Dong[f], Natalie J. Burls[g], Timothy Andrews[h], Daniel E. Amrhein[i], Jiang Zhu[i], Wenhao Dong[j], Yi Ming[k], and Philip Chmielowiec[e]

[a] Department of Atmospheric Sciences, University of Washington, Seattle, WA, USA
[b] School of Oceanography, University of Washington, Seattle, WA, USA
[c] Department of Geosciences, University of Arizona, Tucson, AZ, USA
[d] Department of Geography, University of Cambridge, UK
[e] Department of Atmospheric Sciences and Department of Geology, University of Illinois at Urbana Champaign, Urbana, IL, USA
[f] Lamont-Doherty Earth Observatory, Columbia University, Palisades, NY, USA
[g] Department of Atmospheric, Oceanic, and Earth Sciences, George Mason University, Fairfax, VA, USA
[h] Met Office Hadley Centre, Exeter, UK
[i] Climate and Global Dynamics Laboratory, National Center for Atmospheric Research, Boulder, CO, USA
[j] NOAA/Geophysical Fluid Dynamics Laboratory, Princeton, NJ, USA
[k] Earth and Environmental Sciences and Schiller Institute for Integrated Science and Society, Boston College, Boston, MA, USA

*Corresponding author: Vincent T. Cooper
Email: vcooper@uw.edu

This PDF file includes:

Supporting text
Figures S1 to S22
Tables S1 to S3
SI References

Supporting Information Text

Text S1. Forcing Efficacy and Pattern Effects.

In this section, we briefly consider the relationship between "efficacy" and pattern effects, which is explored in detail in Zhou et al. (2023) (1). The efficacy framework translates one unit of forcing by a non-CO_2 agent, e.g., ice sheets, into the equivalent amount of CO_2 forcing which would cause the same global-mean ΔT. While past research on forcing efficacy has considered that different forcings have different temperature impacts (2), analyses using the efficacy framework for the LGM have produced disparate results (3–8), possibly due to simplified physics of intermediate-complexity models (3, 8). Because of these results, WCRP20 inflates uncertainty on LGM forcings.

Efficacy, ε, can be equivalently framed as a ratio of radiative feedbacks, e.g., $\varepsilon_{IceSheet}=\lambda_{2x}/\lambda_{IceSheet}$. The negative LGM pattern effect ($\Delta\lambda=\lambda_{2x}-\lambda_{LGM}$, $\Delta\lambda<0$), which we find in AGCM simulations using data-assimilation reconstructions for the LGM, is consistent with an LGM efficacy > 1. The efficacy of ice sheets is greater than 1 in the following model-only studies with mixed-layer oceans coupled to atmospheric general circulation models: CESM1-CAM5 (4), CESM2 (7), and CESM2-PaleoCalibr (9) (SI Appendix, Text S2). Some intermediate-complexity models (3, 8), however, have reported ice-sheet efficacy less than 1.

The pattern effect, combined with temperature dependence, can equivalently explain forcing efficacy (1). We use the pattern-effect framework rather than efficacy because it allows for quantification of feedback changes in AGCMs using observational constraints on SST patterns from data assimilation and has strong theoretical underpinnings (1, 10, 11). The pattern-effect framework is oriented around the climate feedback, λ, which is the key uncertain parameter for climate sensitivity. We follow methods in WCRP20 (12) to account for Δλ for the LGM in estimates of modern-day climate sensitivity. We refer readers to Zhou et al. (2023) (1) for further explanation of the connection between efficacy and pattern-effect frameworks.

Text S2. LGM Pattern Effects in Coupled Models.

Simulations with mixed-layer ocean models coupled to AGCMs (known as slab ocean models (13), "SOM" hereafter) in CESM1-CAM5 (4), CESM2.1-CAM6 (7), and CESM2-PaleoCalibr (9) illustrate pattern effects in coupled models. Note that feedbacks from ocean dynamics are excluded in the SOM, and models' SST/SIC patterns are not constrained by proxy data, hence we use the SOM only to support interpretation of the LGM pattern effect. Feedbacks in SOM simulations are calculated as $\lambda=\Delta ERF/\Delta T$, where the effective radiative forcing (ERF) is determined from introducing forcings in separate simulations in the corresponding AGCMs (keeping SST/SIC fixed at pre-industrial values), and ΔT is the equilibrium change in global-mean near-surface air temperature in the SOM (also known as reference-height temperature, or "TREFHT" in CESM name conventions). The ERF is affected by changes in land-surface temperatures, which are not held constant in AGCM simulations due to practical limitations, and an adjustment (2, 4) to the ERF can be made to account for land changes—see Zhu & Poulsen (2021) (4) for methods.

This adjustment, which is based on a climate sensitivity parameter (4) can also be applied to estimate an "adjusted ERF" for LGM ice sheets, although it is difficult to assess the validity of the adjustment for ice-sheet forcing, which affects not only land temperatures but also topography. Radiative kernels based on modern climate would typically be used to validate the ERF adjustment (4), but they cannot be applied with LGM topography. SI Appendix, Figure S11, shows feedbacks from coupled models using both ERF and adjusted ERF. Note that these values do not affect our quantification of Δλ for ECS calculations, which comes from AGCM simulations.

Text S3. Preparation of SST/SIC Boundary Conditions.

SST and SIC boundary conditions (BCs) for the LGM, Late Holocene baseline, and $2xCO_2$ are prepared to enable consistent calculation of the net feedback (λ) that is applicable to a modern-day doubling of CO_2. When changing the surface BCs in AGCM simulations to compute λ, $\Delta F=0$ in Eq. 1 only if there are no changes in land-sea distribution or ice-sheets. For the LGM and Late Holocene datasets, we adjust for differences in land-sea distribution, determined from refs. (14, 15), compared to present day using kriging and extrapolation near coastlines in polar regions. While sea-level changes must be neutralized to preserve ΔF=0 in the AGCM simulations, infilling SST over the Sunda Shelf represents a notable uncertainty (16, 17). The alternative option, holding all forcings constant at LGM rather than modern values, would require changing modern topography to include LGM ice sheets and inherit sea level of the LGM. Those changes could introduce more uncertainty in estimates of λ that are relevant to future warming. Here we only consider the framework with constant modern-day forcings.

For SST, kriging is performed across overlapping subset regions of radius≈3000 km spaced around the globe. Results for overlapping subset regions are merged using inverse-distance weighting from the center of each subset region. Kriging results are retained only where no pre-existing SST value exists in a dataset. Over polar regions and inland waters, inverse-distance extrapolation populates the SST field.

For SIC, all values are first required to be no less than the ice-sheet fraction at that location, i.e., modern seas that were covered by ice sheets at the LGM, such as the Hudson Bay, are assigned a minimum SIC that equals the LGM ice fraction at 21,000 years ago (14, 15). For modern seas which were land but not ice sheet at the LGM, SIC is populated based on the SST. This step uses the SIC formula from the CAM boundary condition protocol (18), where SIC=100% if SST<–1.8°C, SIC=0% if SST>4.97°C, and otherwise the infilled $SIC=0.729-((SST+1.8)/9.328)^{1/3}$. Gaussian smoothing is applied to the result, reducing any sharp boundaries caused by the infilling. The SIC formula above is also applied to maintain internally consistent values of SST and SIC (18) in the Late Holocene baseline. See SI Appendix, Text S4, for uncertainty tests regarding sea ice.

The Annan dataset includes only annual SST and no reconstruction of SIC. Because SIC is required in all AGCMs, we assign the SIC from Amrhein to the Annan data. In a CAM4 test using the LGMR SIC with Annan SSTs (instead of the Amrhein SIC), Δλ is marginally more negative (λ_{LGM} changes by < 0.1 $Wm^{-2}K^{-1}$). This result suggests that uncertainty from assigning a SIC reconstruction to Annan SSTs is small compared to uncertainty in the SST reconstruction. We assign the Amrhein SIC for the Annan SST in our main results because this choice is more conservative in that it reduces the magnitude of the mean LGM pattern effect. For consistency, the Annan SST is assigned the annual cycle from the Amrhein data for SST/SIC.

For the $2xCO_2$ BC, we use output from LongRunMIP (19) simulations of abrupt and transient-1% yr^{-1} doubling of CO_2. We use the mean of 200 years of output from the following six models in to create a multi-model mean SST/SIC BC: CESM1.0.4 (20) years 2300–2500, CNRM-CM6-1 (21) years 550–750, HadCM3L (22) years 500–700, MPI-ESM-1.2 (23) years 800–1000, GFDL-ESM2M (24) years 4300–4500, and MIROC3.2 (25, 26) years 1803–2003. HadCM3L results use years 500-700 due to an output error in the pre-industrial control run after year 700. All LongRunMIP results are regridded to a standard 1.9º x 2.5º lat-lon grid. For SIC, monthly output is available, and we compute a 200-yr climatology for each model and then a multi-model-mean climatology. For SST, annual output is available for each model and monthly output from MIROC3.2. We compute the 200-yr mean SST anomaly for each model and then apply the annual cycle from MIROC3.2 to the multi-model mean. We also show results in SI Appendix, Fig. S3–S4, which do not use the LongRunMIP-$2xCO_2$ BC and instead use 150-year regressions (27) of abrupt-$4xCO_2$ from parent coupled models corresponding to each AGCM used in this study, thereby sampling uncertainty in warming patterns because the 150-year regressions are produced from different models' warming patterns.

BCs are regridded to the 1.9° x 2.5° (latitude x longitude) grid used for CAM4, CAM5, and CAM6. HadGEM3-GC31-LL regrids to N96 (resolution of approximately 135 km) (28), and GFDL-AM4 regrids to a C96 cubed sphere (resolution of approximately 100 km) (29).

For the "pattern-only" simulations with SST anomalies normalized to −0.5 K, we make the following changes to the LGM and $2xCO_2$ BCs. For the LGM, we use the LGMR SST. For $2xCO_2$, we use the LongRunMIP SST. We compute the global-mean ΔSST for both datasets as $\overline{\Delta SST}$, and we multiply all local SST anomalies by the scale factor $-0.5/\overline{\Delta SST}$. This scaling causes the resulting global-mean ΔSST to become −0.5 K, but the spatial pattern of the SST anomalies is unchanged. We use −0.5 K for both the LGM and $2xCO_2$ so that there is no cooling-warming asymmetry, and ΔT is small enough that temperature dependence of λ is negligible (i.e., $\Delta\lambda_T \approx 0$, and $\Delta\lambda \approx \Delta\lambda_{PatternOnly}$). ΔT is still large enough that we can compute λ=ΔN/ΔT without requiring an excessively long simulation to overcome noise in the denominator. We use the baseline SIC (Late Holocene) in all of the pattern-only simulations so there are no changes in sea ice, so this set of simulations also serves to check whether $\Delta\lambda$ is attributable to SIC rather than SST changes.

To examine whether the pattern-only results are sensitive to the scaling method of separating pattern effects, we tested an alternative subtraction method in CAM4 (using the LGMR pattern for the LGM and the LongRunMIP pattern for $2xCO_2$). We ran alternative pattern-only simulations with global-mean SST anomalies set to zero by subtracting the global mean at all locations. These experiments produced consistent results for $\Delta\lambda_{PatternOnly}$ compared to scaling.

An additional simulation was run in HadGEM3-GC3.1-LL with SIC held constant at the Late Holocene baseline while the SST field is varied with the full value of anomalies, using the LongRunMIP-$2xCO_2$ and LGMR patterns of SST. Results from this simulation are shared in SI Appendix, Text S4.

This concludes the preparation steps for the main simulations (BCs from four data-assimilation reconstructions for the LGM, one Late Holocene, and one $2xCO_2$) and the “pattern-only” simulations (two additional BCs: LGMR and LongRunMIP-$2xCO_2$ scaled to −0.5 K). The final adjustment to each BC follows the standard boundary-condition protocol for CAM, known as “bcgen.” This process ensures that SIC and SST are plausibly bounded (e.g., SIC between 0 and 1), and it transfers the monthly climatology to mid-month values which can be linearly interpolated in an AGCM.

Text S4. Uncertainty of $\Delta\lambda$.

To include the LGM pattern effect in the Bayesian framework of WCRP20, we must assign a statistical distribution to $\Delta\lambda$ for the LGM (following WCRP20’s method for $\Delta\lambda$ in the historical record). In this section we provide additional detail on combining uncertainty from AGCM physics and LGM reconstructions with bootstrapping.

To evaluate the sensitivity of our uncertainty quantification to the size of our sample of AGCMs and reconstructions, we calculate a bootstrap confidence interval (CI) on our estimate, $\hat{\sigma}$, of the standard deviation of $\Delta\lambda$ as follows. First, we construct a sample where each AGCM is equally weighted and the spread from various LGM reconstructions is included in the sample (as described below). We then use bootstrapping of this sample to provide confidence bounds on our estimate ($\hat{\sigma}$) of the population standard deviation from the sample standard deviation.

To create the equally weighted sample, we assume that the spread around the LGMR feedback (of the feedbacks from Amrhein, Annan, and lgmDA) would be the same in GFDL-AM4, HadGEM3-GC3.1-LL, and CAM6 as they are in CAM4 or CAM5. We include the simulations using the extreme quartiles from Annan and LGMR in the sample. This assumption yields a sample of 40 values of $\Delta\lambda$ based on (4 LGM patterns + 2 extreme-quartile LGMR patterns + 2 extreme-quartile Annan patterns) x (5 AGCMs). We proceed with bootstrapping by sampling with replacement from the 40 values of $\Delta\lambda$. We generate 10^5 samples of size n=19, choosing this sample size for the bootstrap because there are 19 direct estimates of $\Delta\lambda$ from simulations in the AGCMs. This process yields 10^5 bootstrapped values of $\hat{\sigma}$ from which we derive the 95% CI: (0.15, 0.31) $Wm^{-2}K^{-1}$. Note that the upper bound of 0.31 $Wm^{-2}K^{-1}$ is much less than two times the population standard deviation of 0.23 $Wm^{-2}K^{-1}$ that we assign to $\Delta\lambda$, indicating that doubling the assumed standard deviation for $\Delta\lambda$ is a more conservative uncertainty test (SI Appendix, Fig. S4) than using the bootstrapped 95% bound.

To determine the distribution of $\Delta\lambda$ in SI Appendix, Figure S4, we repeat the bootstrap estimate using $\lambda_{4x(150yr)}/1.06$ instead of λ_{2x}, where 1.06 represents WCRP20’s central estimate (12) for the timescale adjustment between the 150-year feedback and the equilibrium feedback; this yields $\overline{\Delta\lambda}=-0.27\ Wm^{-2}K^{-1}$ and mean sample standard deviation of 0.20 $Wm^{-2}K^{-1}$.

Our method of combining uncertainty gives equal weight to the most-extreme quartiles and to the central estimates, but this overestimate of uncertainty is warranted given that paleoclimate data assimilation may underestimate the true uncertainty (30). The uncertainty estimate also gives more weight to the most recent reconstructions, LGMR (31) and Annan (32), by including three simulations (mean, 1st quartile, and 4th quartile) from these datasets. The weighting influences the bootstrap estimate and the distribution assigned to $\Delta\lambda$ in our calculations of ECS.

Over the range of temperatures between the LGM and $2xCO_2$, all five AGCMs appear to have weaker temperature dependence of feedbacks than WCRP20 assumes, i.e., $\Delta\lambda_T$ appears smaller than in WCRP20. $\Delta\lambda_T$ could be underestimated in all models, so we include an uncertainty test where we use the pattern-only simulations in CAM4, CAM5, and CAM6 to estimate the mean $\Delta\lambda_{PatternOnly}$ contribution to the total $\Delta\lambda$, and we retain WCRP20's estimate of $\Delta\lambda_T$. In this uncertainty test, $\Delta\lambda$ in Eq. 6 is calculated as the sum of $\Delta\lambda_T$ and $\Delta\lambda_{PatternOnly}$: $\Delta\lambda_T=-\alpha\Delta T/2$ with $\alpha \sim N(0.1, 0.1)$ $Wm^{-2}K^{-2}$ as in WCRP20, while $\Delta\lambda_{PatternOnly} \sim N(-0.51, 0.23)$ $Wm^{-2}K^{-1}$ with μ based on CAM4, CAM5, and CAM6 results (SI Appendix, Table S3). The results of this uncertainty test are included in SI Appendix, Figure S9, indicating that accounting for pattern effects causes the dominant change to LGM evidence for ECS, while the revision to WCRP20's temperature dependence contributes a smaller portion of the update.

Sea-ice reconstructions, which are not well constrained, contribute to uncertainty in the LGM pattern effect. However, the uncertainty due to sea ice appears small compared to the uncertainty across AGCM physics and in the SST pattern. In an additional set of simulations with HadGEM3-GC3.1-LL, the SST anomalies are applied in full at the LGMR, Late Holocene, and LongRunMIP-2xCO_2 values while the SIC is held constant at the Late Holocene values. These simulations make λ_{2x} and λ_{LGM} more negative by eliminating the positive ice-albedo feedback, but the difference in the feedbacks, $\Delta\lambda$, is largely unaffected. Constant SIC produces $\Delta\lambda = -0.28$ $Wm^{-2}K^{-1}$, compared to -0.27 $Wm^{-2}K^{-1}$ in the main simulations for HadGEM3-GC3.1-LL. SIC is also held constant in the pattern-only simulations, which produce $\Delta\lambda<0$. While our results appear robust despite uncertainty in SIC, substantially different LGM reconstructions or SIC responses to modern-day 2xCO_2 could change the resulting $\Delta\lambda$. Future work should continue investigating the role of sea ice in paleoclimate pattern effects.

Text S5. Zonal-mean Feedbacks.

SI Appendix, Figures S12–S22 show zonal means (indicated by brackets as [λ]) of the global-mean feedbacks that appear in SI Appendix, Figure S6. The net feedback, clear-sky shortwave (SW), clear-sky longwave (LW), and cloud radiative effect are calculated directly from model output. The remaining feedbacks are from radiative kernel decomposition (Materials and Methods) using CAM5 kernels (33, 34). GFDL-AM4's 2xCO_2 simulation has error in the kernel-derived clear-sky feedback equal to 15.6% of the actual feedback, exceeding the 15% threshold commonly used as a test of clear-sky linearity (35–37); all other simulations have clear-sky feedback errors less than 10%. Total cloud feedback is also shown as the sum of kernel-derived SW and LW components.

Each of the zonal-mean figures consists of: (A) In CAM5, mean and range of feedbacks across four LGM reconstructions and 2xCO_2 from LongRunMIP. (B) In CAM5, mean and range of the difference in feedbacks ($\Delta\lambda = \lambda_{2x} - \lambda_{LGM}$) across four LGM reconstructions from results in panel A. (C) Feedbacks across various AGCMs, using the LGMR reconstruction of the LGM and 2xCO_2 from LongRunMIP. (D) Mean and range of $\Delta\lambda$ across various AGCMs from results in panel C. Note that HadGEM3 is not included in the kernel-derived feedbacks due to limited availability of model output.

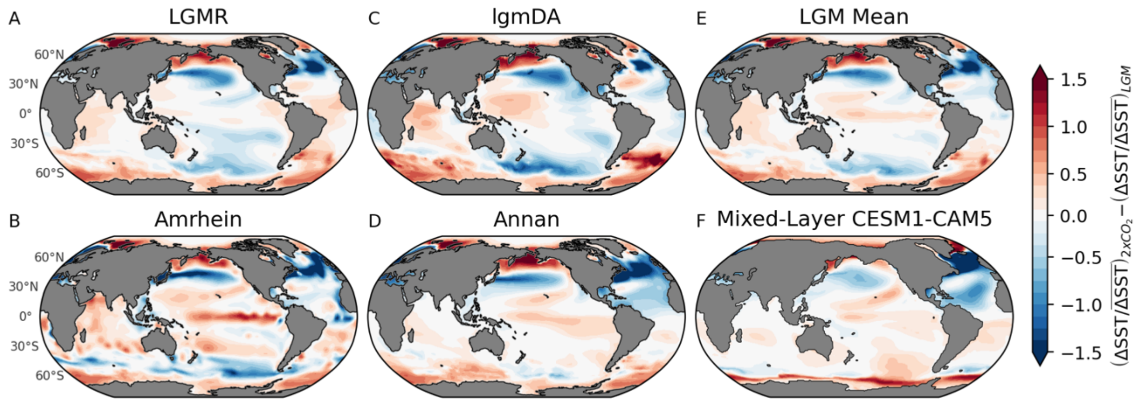

Fig. S1. Differences in LGM sea-surface temperature (SST) patterns compared to $2xCO_2$ reference pattern. All local anomalies are normalized through division by global-mean anomaly, then differences between the $2xCO_2$ pattern and LGM pattern are taken. Red regions indicate where SST anomalies are relatively more amplified in $2xCO_2$, while blue regions indicate where SST anomalies are relatively more amplified at the LGM. (A–E), LGM patterns corresponding to Fig. 1A–E, and $2xCO_2$ reference pattern is Fig. 1F from LongRunMIP-$2xCO_2$. (F) In CESM1-CAM5 (4) mixed-layer ocean model without data assimilation, difference between $2xCO_2$ and LGM patterns (shown in SI Appendix, Figure S5C–D).

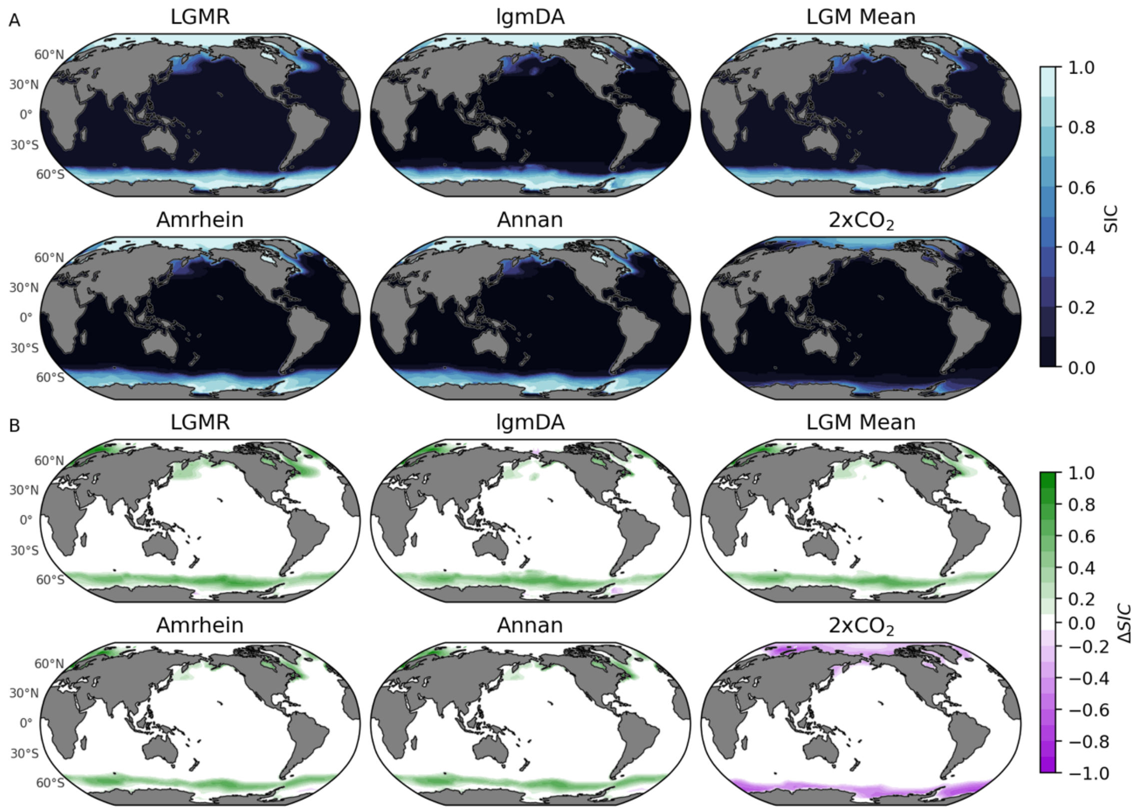

Fig. S2. Sea-ice concentration (SIC) from data-assimilation reconstructions of the Last Glacial Maximum (LGM) compared to $2xCO_2$. **(A)** SIC from LGM Reanalysis (LGMR) (31), Amrhein (38), lgmDA (39), Annan (32) (assigned SIC from Amrhein); mean of three LGM reconstructions (LGMR, Amrhein, and lgmDA); and multi-model mean from near-equilibrium simulations of $2xCO_2$ in LongRunMIP (19), where each of six models is averaged over final 200 years of simulation. (B) Difference in sea-ice concentration relative to Late Holocene baseline (LGMR reconstruction). All panels show annual mean. Reconstructions are infilled to modern coastlines (Materials and Methods).

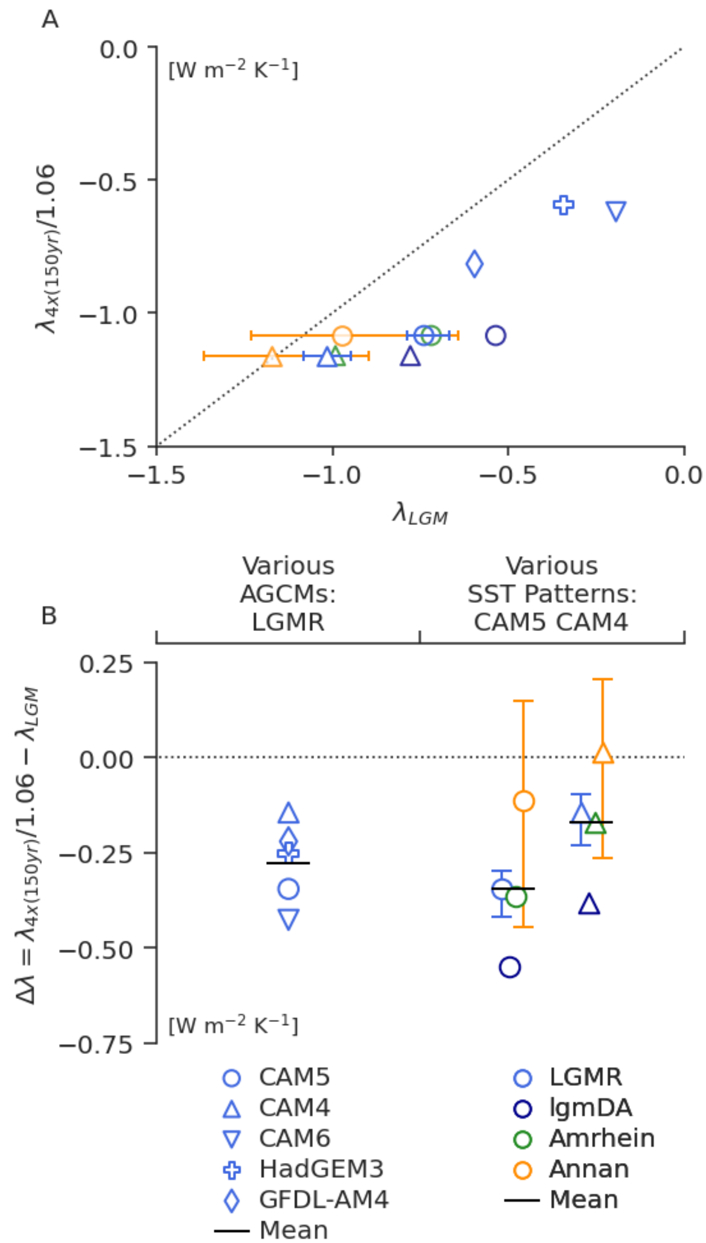

Figure S3. Last Glacial Maximum (LGM) pattern effect ($\Delta\lambda$) based on LGM climate feedbacks in AGCMs and CO_2 climate feedbacks from 150-yr regression of abrupt-4xCO_2 in coupled models. Identical to Fig. 2, except λ_{2x} is replaced by $\lambda_{4x(150yr)}/1.06$, the feedback from regression in abrupt-4xCO_2 simulations (27) using parent coupled models corresponding to each AGCM; a timescale adjustment of 1/1.06 is applied based on the WCRP20 central estimate (12) to make 150-year 4xCO_2 feedbacks comparable with λ_{LGM} equilibrium feedbacks. Different models (all using the LGMR pattern for the LGM) are indicated by symbols. Different LGM patterns (in CAM5 and CAM4) are indicated by colors. (A) Scatter plot of 4xCO_2 feedbacks (including adjustment factor of 1/1.06) versus LGM feedbacks, with $\lambda_{4x(150yr)}/1.06=\lambda_{LGM}$ shown as dashed line. (B) LGM pattern effect, $\Delta\lambda= \lambda_{4x(150yr)}/1.06-\lambda_{LGM}$, using feedbacks shown in panel A, with $\Delta\lambda=0$ shown as dashed line.

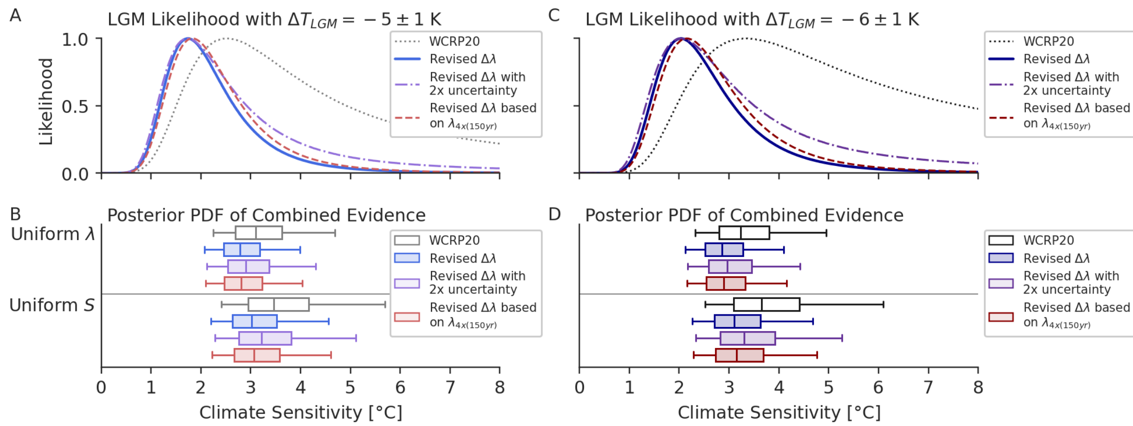

Figure S4. Uncertainty tests for modern-day climate sensitivity including the LGM pattern effect. Following Fig. 4, showing WCRP20 original (12) LGM ΔT_{LGM}~ N(μ=−5, σ=1) K in left column and revised LGM ΔT_{LGM}~N(−6, 1) K based on IPCC AR6 (40) in right column, including two uncertainty tests. Results from WCRP20 (12) with no LGM pattern effect (gray and black) and our base assumption (light and dark blue) for revised Δλ~N(−0.37, 0.23) $Wm^{-2}K^{-1}$ from Fig. 4 are repeated here for comparison. First uncertainty test (light and dark purple) increases the σ assumption by a factor of two: Δλ~N(−0.37, 0.46) $Wm^{-2}K^{-1}$. Second uncertainty test (light and dark red) concerns the $2xCO_2$ pattern and feedback: a different distribution, Δλ~N(−0.27, 0.20) $Wm^{-2}K^{-1}$, is assigned based on results shown in Ext. Data Fig. 3 using $\lambda_{4x(150yr)}/1.06$, the feedback derived from 150-year regressions (27) of abrupt-$4xCO_2$ using parent coupled models corresponding to each AGCM, including a timescale-adjustment factor of 1/1.06 from WCRP20's central estimate (12). Climate sensitivity shown is effective sensitivity (S) from 150-year response, as in WCRP20 (12). (A) Likelihood functions for S based on only the LGM line of evidence. (B) Posterior PDF after combining LGM with other lines of evidence in WCRP20 (12), assuming a uniform-λ prior (upper panel) or a uniform-S prior (lower panel). Outlier lines indicate 5–95th percentiles, and box indicates 25–75th percentiles and median.

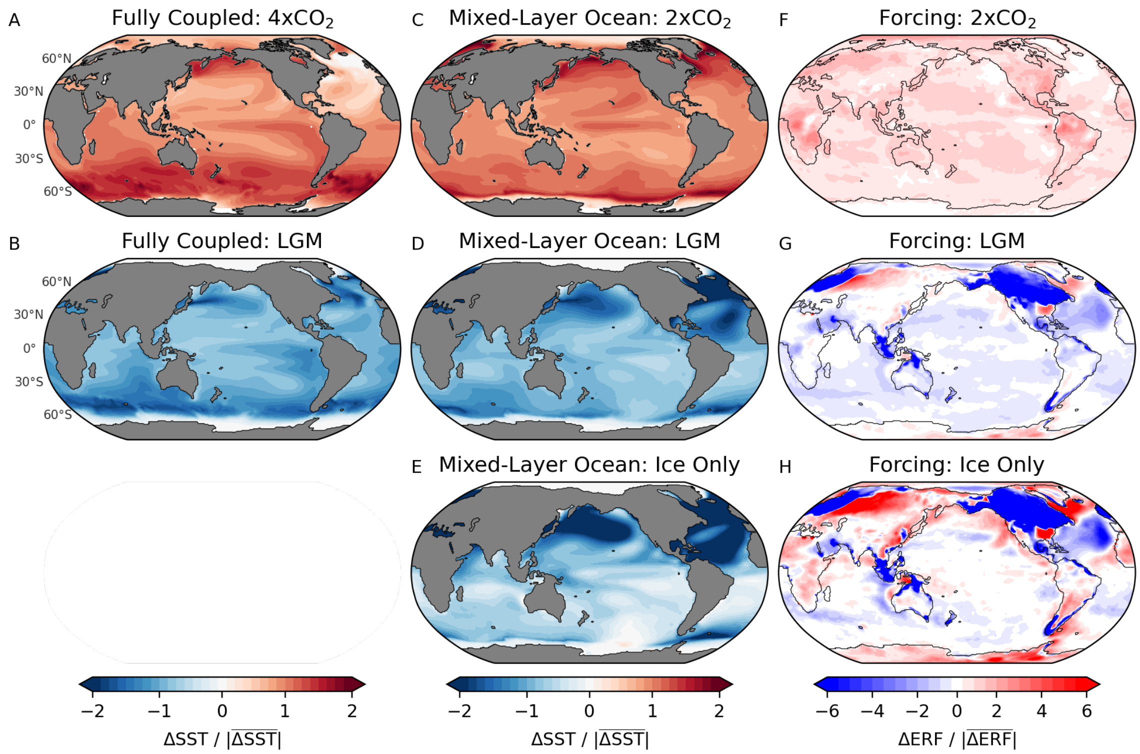

Figure S5. Spatial patterns of sea-surface temperature (SST) response and effective radiative forcing (ERF) in CESM1-CAM5 model simulations from Zhu & Poulsen (4). Spatial patterns here are shown as zonal means in Fig. 2. All local anomalies are normalized through division by absolute value of global-mean anomaly. (A–B) SST patterns in quasi-equilibrium from fully coupled atmosphere-ocean model with LGM ice-sheet and greenhouse-gas forcings (4) compared to abrupt-4xCO_2 forcing (41). (C–E) Equilibrium SST patterns from mixed-layer ocean model coupled to CAM5, including a simulation with only LGM ice-sheet forcing (4). (F–H) ERF patterns from corresponding AGCM simulations in CAM5.

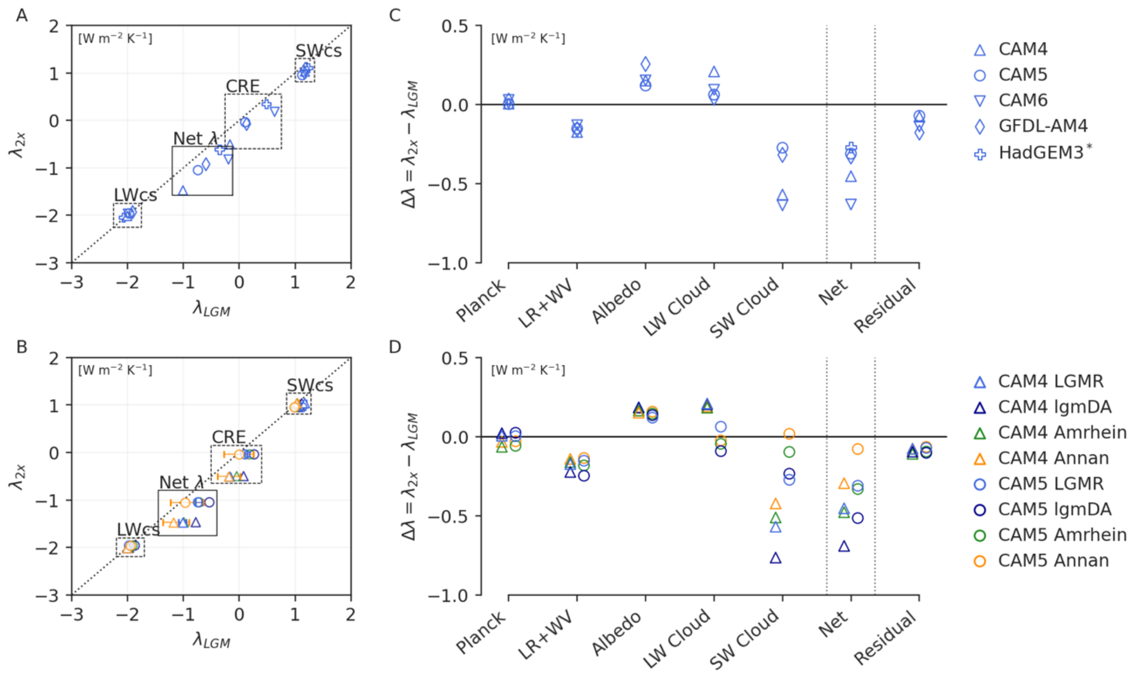

Figure S6. Feedback decomposition of Last Glacial Maximum (LGM) and $2xCO_2$ climate feedbacks in atmospheric general circulation models (AGCMs). Left column uses direct model outputs in scatter plots of $2xCO_2$ feedbacks (λ_{2x}) versus LGM feedbacks (λ_{LGM}), with $\lambda_{2x}=\lambda_{LGM}$ denoted by dashed line. Cloud radiative effect (CRE), shortwave clear-sky (SWcs), longwave clear-sky (LWcs), and net feedbacks are shown. (A) Results from various AGCMs, all using the LGMR reconstruction for the LGM. (B) Results from various LGM reconstructions in CAM4 and CAM5, with different reconstructions indicated by colors. Right column shows decomposition of $\Delta\lambda$ using CAM5 radiative kernels (34), with residual equal to the net feedback in models minus the sum of kernel-derived feedbacks. (C) Results from various AGCMs (note that only net λ is available for HadGEM3). (D) Results from various LGM reconstructions in CAM4 and CAM5. Lapse rate and water vapor feedbacks are combined (LR+WV) given their anti-correlation across models (42).

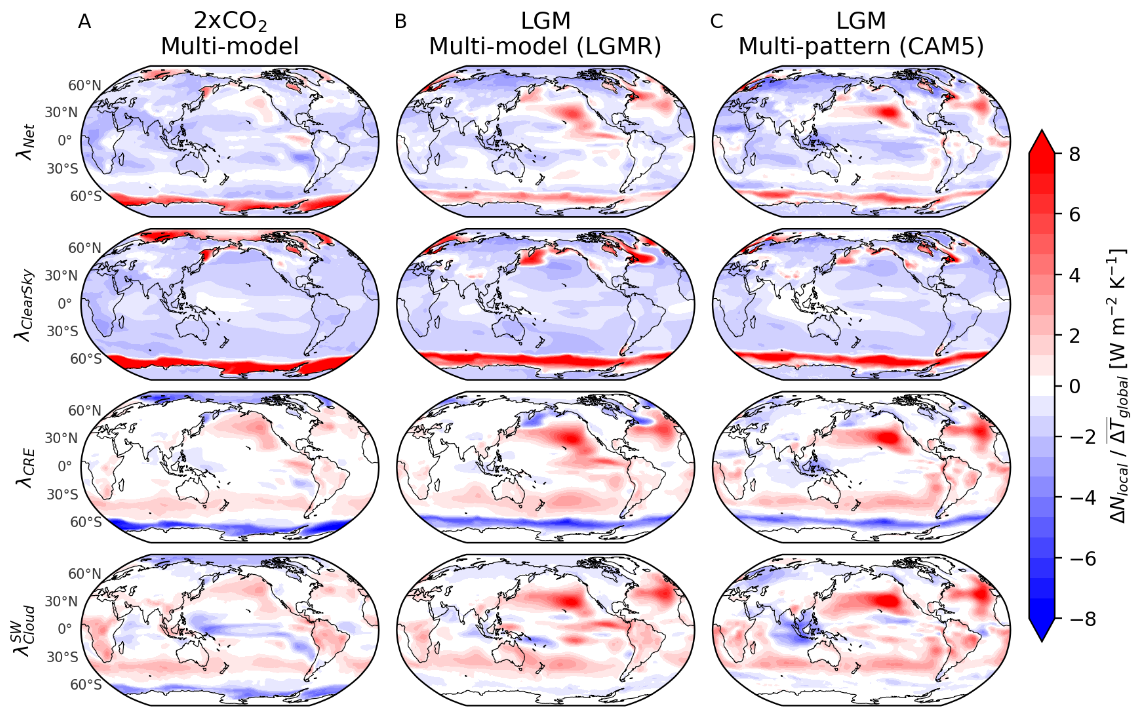

Figure S7. Spatial decomposition of Last Glacial Maximum (LGM) and $2xCO_2$ local climate feedbacks in atmospheric general circulation models (AGCMs). Local feedbacks represent local change in top-of-atmosphere radiation (ΔN_{local}) divided by global-mean change in near-surface air temperature (ΔT_{global}); global integrals of the local feedbacks equal the global-mean feedbacks. Top row shows net feedback (λ_{Net}) from total all-sky changes in ΔN, second row shows $\lambda_{ClearSky}$ from changes in ΔN attributable to clear-sky radiation, third row shows cloud radiative effects (λ_{CRE}); rows 1–3 use direct model output. Fourth row shows radiative-kernel estimates of shortwave cloud feedbacks (λ^{SW}_{Cloud}). (A) $2xCO_2$ multi-model mean based on five AGCM simulations using LongRunMIP (19) pattern. (B) LGM multi-model mean based on five AGCM simulations using LGMR (31) pattern. (C) LGM multi-pattern mean in CAM5 using four LGM reconstructions. Note that radiative-kernel results for λ^{SW}_{Cloud} exclude HadGEM3 due to output limitations.

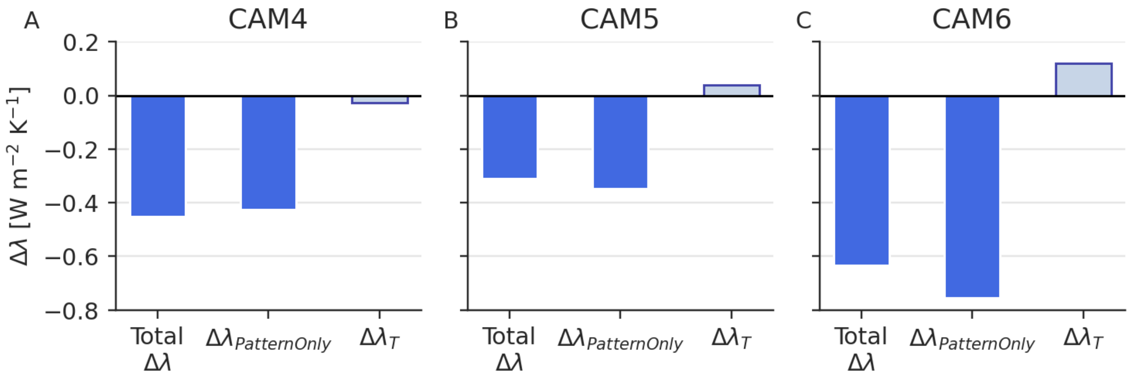

Figure S8. Separating pattern and temperature dependence of feedback changes as total $\Delta\lambda \approx \Delta\lambda_{PatternOnly} + \Delta\lambda_T$. First column shows total $\Delta\lambda = \lambda_{2x} - \lambda_{LGM}$ from Figure 2, calculated in main simulations with full SST anomalies and SIC for 2xCO_2 and LGM (using LGMR reconstruction). Second column shows pattern-only simulations with global-mean ΔSST scaled to −0.5 K, where $\Delta\lambda_{PatternOnly} \approx \lambda_{2x}^{-0.5\mathrm{K}} - \lambda_{\mathrm{LGM}}^{-0.5\mathrm{K}}$. Third column shows temperature dependence, $\Delta\lambda_T$, approximated as the residual difference between the main and pattern-only simulations, $\Delta\lambda_T \approx \Delta\lambda - \Delta\lambda_{PatternOnly}$. Results in (A) CAM4, (B) CAM5, and (C) CAM6.

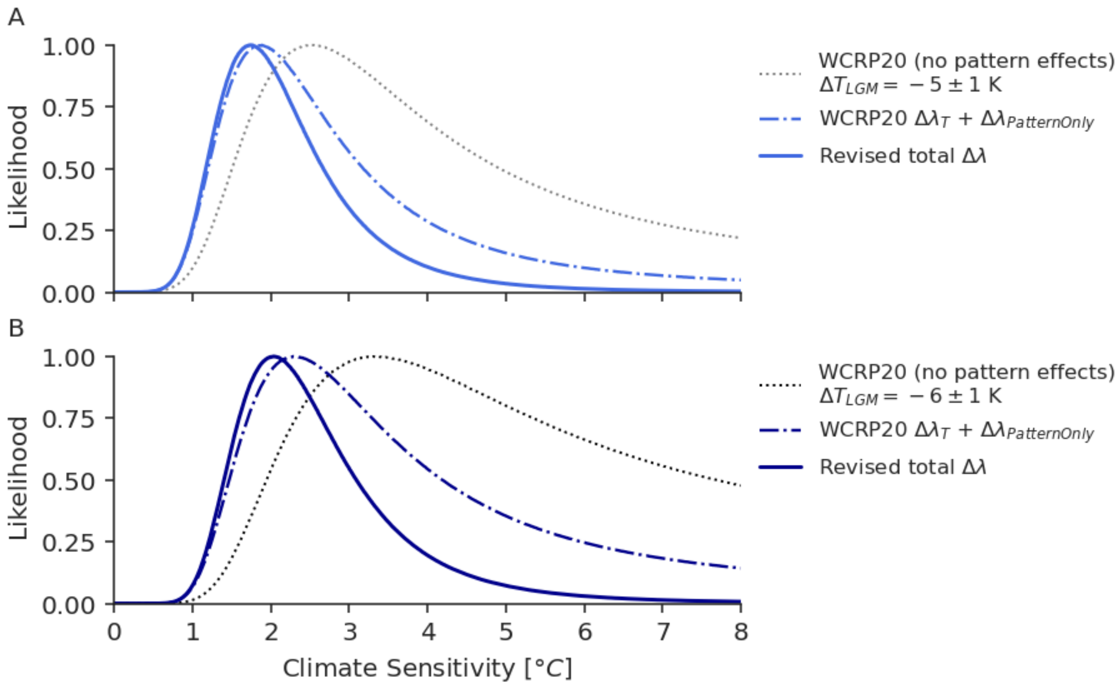

Figure S9. Likelihoods for LGM line of evidence with separate updates for SST pattern effects and temperature dependence of feedbacks. (Dotted) WCRP20 LGM likelihood (12), which includes an estimate of $\Delta\lambda_T$ for the LGM but no adjustment for pattern effects. (Dash-dot) Revised likelihood using WCRP20 estimate of $\Delta\lambda_T$ but including feedback changes from SST patterns based on pattern-only simulations in this study, assuming $\Delta\lambda_{PatternOnly} \sim N(\mu=-0.51, \sigma=0.23)$ $Wm^{-2}K^{-1}$. (Solid) Revised likelihood using total revised $\Delta\lambda$ from this study, as shown in Fig. 4, which includes both pattern effects and temperature dependence, assuming $\Delta\lambda \sim N(-0.37, 0.23)$ $Wm^{-2}K^{-1}$. (A) All likelihoods assume $\Delta T_{LGM} \sim N(-5, 1)$ K as in original WCRP20 results (12). (B) All likelihoods assume $\Delta T_{LGM} \sim N(-6, 1)$ K, using the updated central estimate from IPCC AR6 (40).

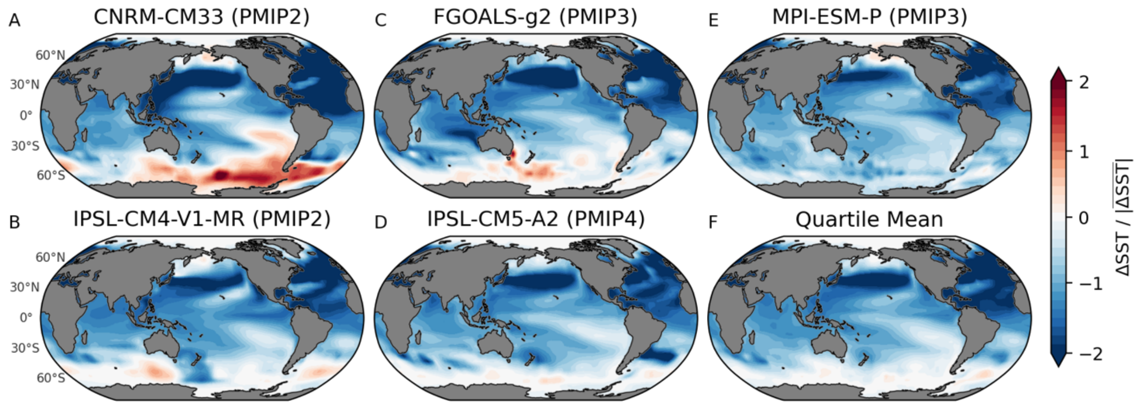

Figure S10. Patterns of SST anomalies from Annan (32) ensemble members in quartile with strongest negative climate feedback (λ). 19 ensemble members are ranked by estimated λ, which is produced from CAM5 Green's functions (10), and 5 members shown comprise the quartile with most-negative estimated λ. (A–E) Data-assimilation posterior SST using model priors specified in subtitles. (F) Pattern of the quartile-mean SST. To show SST patterns, local SST anomalies are normalized into patterns through division by absolute value of global-mean SST anomaly (consistent with feedbacks being radiative responses divided by global-mean temperature anomalies). All panels show annual means. LGM reconstructions are infilled to modern coastlines (Materials and Methods).

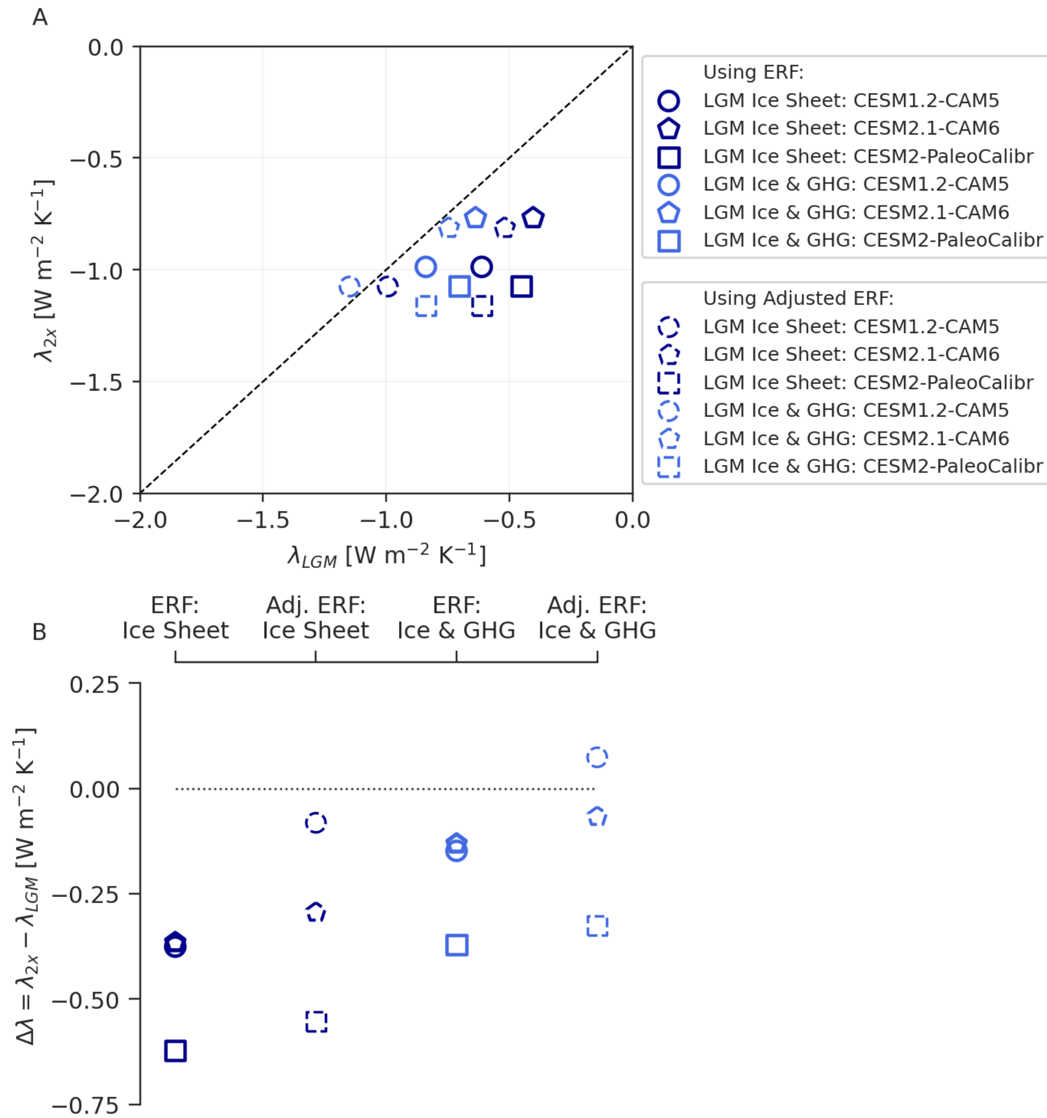

Figure S11. Feedbacks and Δλ using either effective radiative forcing (ERF) or adjusted ERF from previously published simulations in mixed-layer ocean models. (A) Scatter plot of λ_{2x} vs. λ_{LGM} in mixed-layer ocean models; λ_{LGM} is shown for simulations using only the LGM ice-sheet forcing (dark blue), which includes LGM sea-level changes, and for simulations using LGM ice-sheet forcing and greenhouse-gas (GHG) forcings (royal blue). Dashed markers indicate corresponding results using “adjusted ERF” to calculate feedbacks. (B) Δλ based on feedbacks shown in panel A. Note that in LGM simulations using CESM2.1-CAM6 (7) and CESM2-PaleoCalibr (9), the LGM ice-sheet forcing and GHG forcing are applied in separate simulations, and their sums are shown as LGM Ice & GHG. This linearity assumption was validated in CESM1-CAM5 (4).

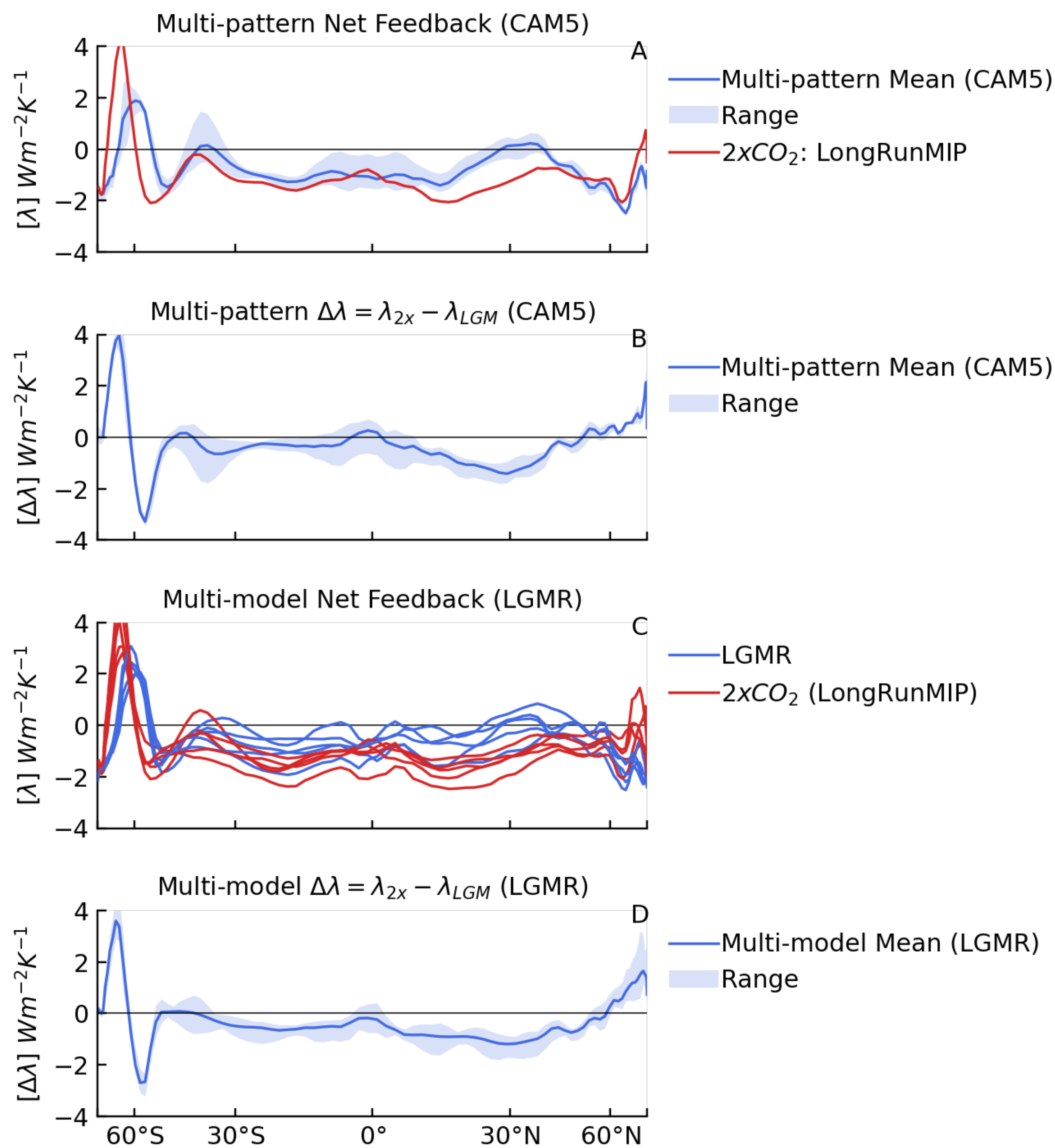

Figure S12. Zonal-mean net feedback and Δλ. (A) In CAM5, mean and range of feedbacks across four LGM reconstructions and $2xCO_2$ from LongRunMIP. (B) In CAM5, mean and range of the difference in feedbacks ($\Delta\lambda = \lambda_{2x} - \lambda_{LGM}$) across four LGM reconstructions from results in panel A. (C) Feedbacks across various AGCMs, using the LGMR reconstruction of the LGM and $2xCO_2$ from LongRunMIP. (D) Mean and range of Δλ across various AGCMs from results in panel C. Note that HadGEM3 is not included in the kernel-derived feedbacks due to limited model output.

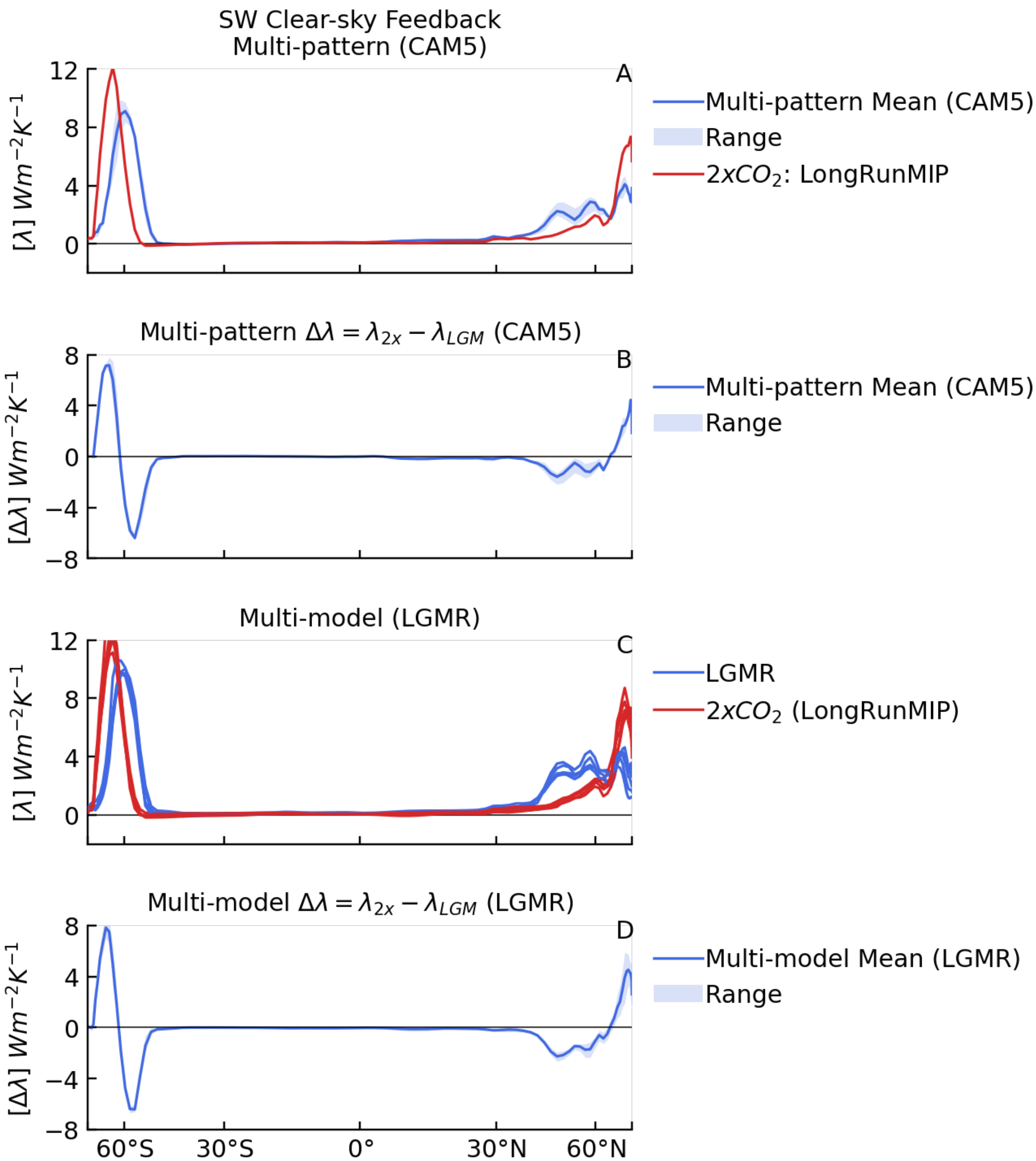

Figure S13. Zonal-mean shortwave clear-sky feedback and Δλ. (A) In CAM5, mean and range of feedbacks across four LGM reconstructions and $2xCO_2$ from LongRunMIP. (B) In CAM5, mean and range of the difference in feedbacks ($\Delta\lambda = \lambda_{2x} - \lambda_{LGM}$) across four LGM reconstructions from results in panel A. (C) Feedbacks across various AGCMs, using the LGMR reconstruction of the LGM and $2xCO_2$ from LongRunMIP. (D) Mean and range of Δλ across various AGCMs from results in panel C. Note that HadGEM3 is not included in the kernel-derived feedbacks due to limited model output.

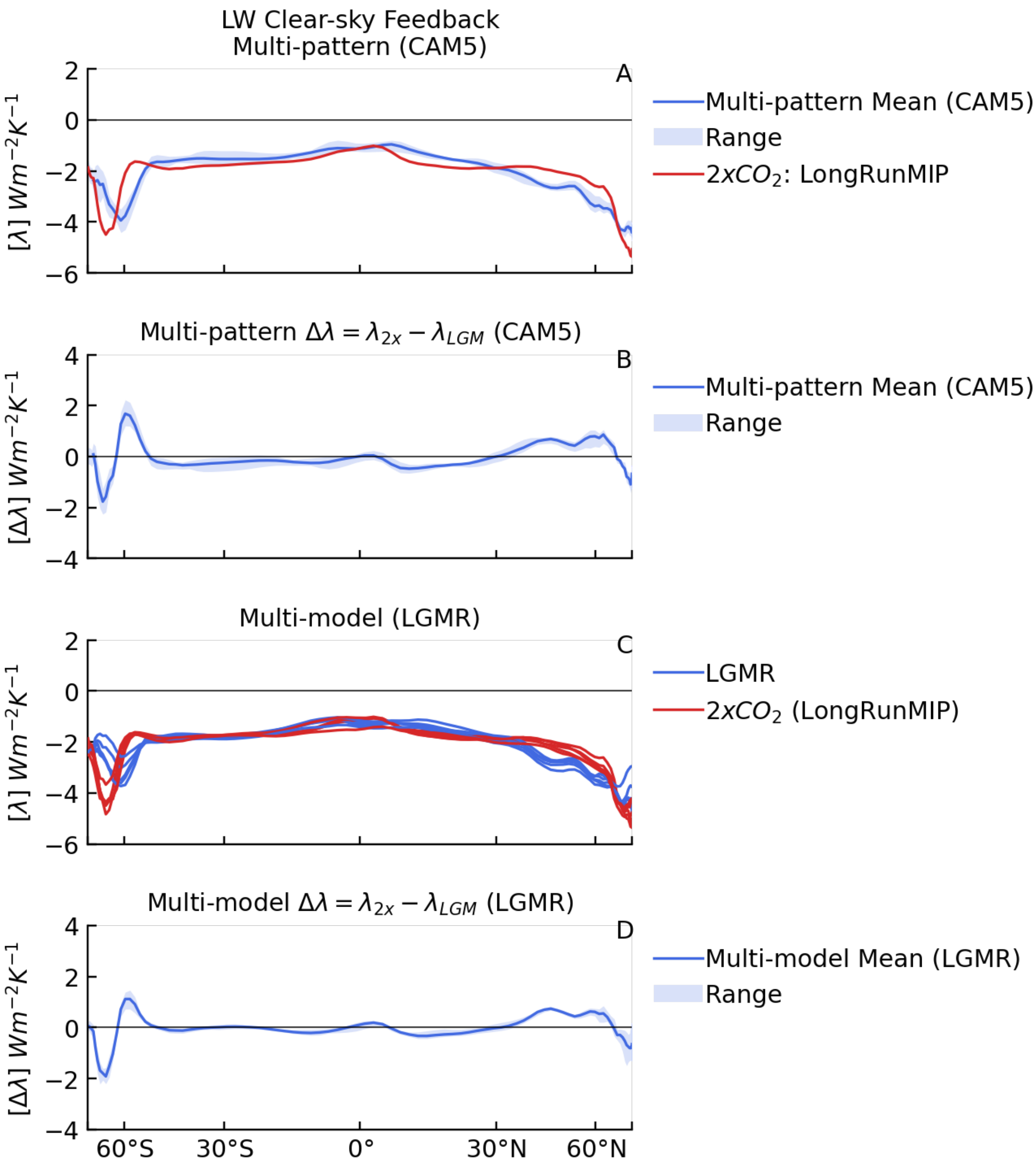

Figure S14. Zonal-mean longwave clear-sky feedback and Δλ. (A) In CAM5, mean and range of feedbacks across four LGM reconstructions and $2xCO_2$ from LongRunMIP. (B) In CAM5, mean and range of the difference in feedbacks ($\Delta\lambda = \lambda_{2x} - \lambda_{LGM}$) across four LGM reconstructions from results in panel A. (C) Feedbacks across various AGCMs, using the LGMR reconstruction of the LGM and $2xCO_2$ from LongRunMIP. (D) Mean and range of Δλ across various AGCMs from results in panel C. Note that HadGEM3 is not included in the kernel-derived feedbacks due to limited model output.

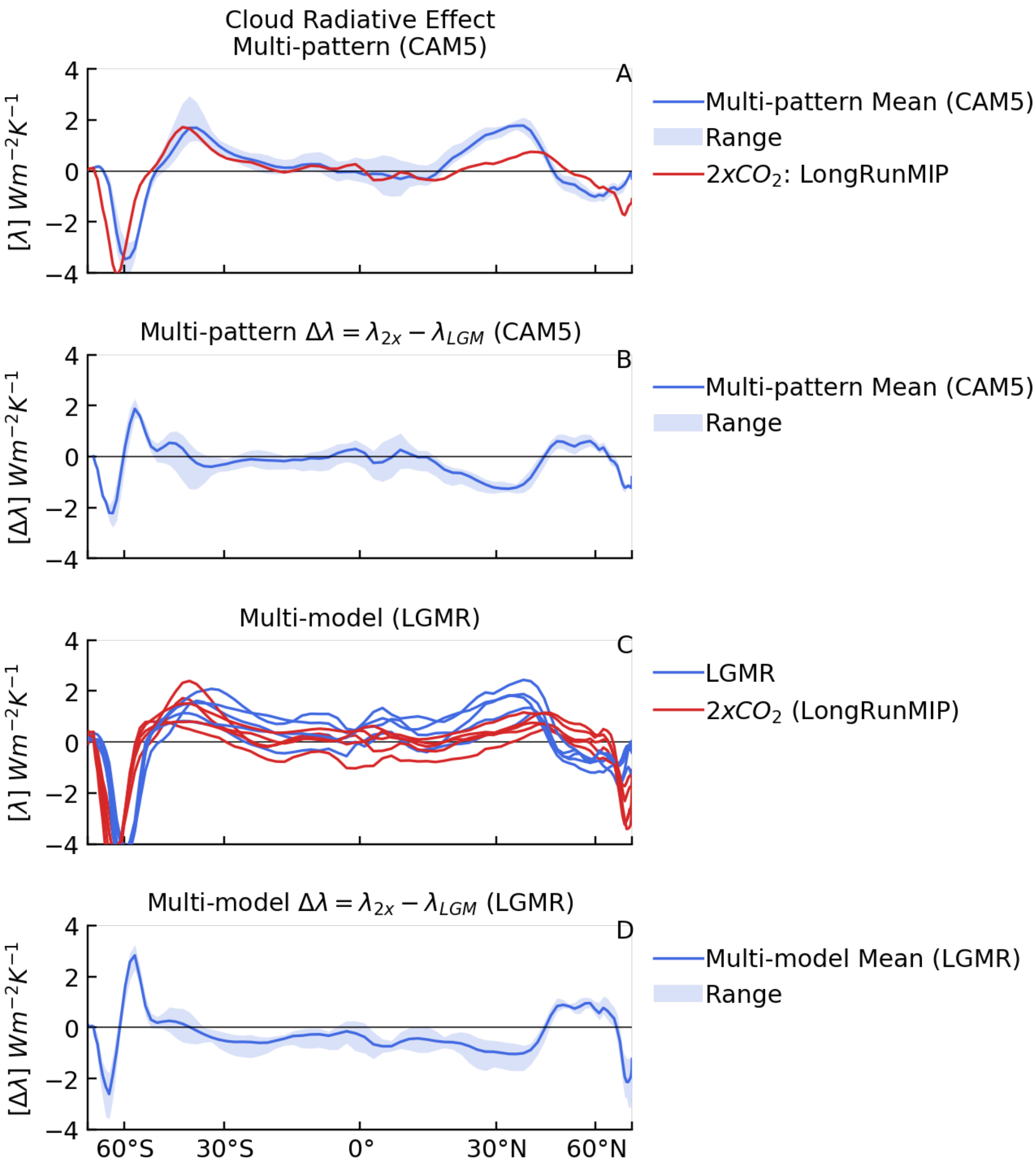

Figure S15. Zonal-mean cloud radiative effect and Δλ. (A) In CAM5, mean and range of feedbacks across four LGM reconstructions and $2xCO_2$ from LongRunMIP. (B) In CAM5, mean and range of the difference in feedbacks ($\Delta\lambda = \lambda_{2x} - \lambda_{LGM}$) across four LGM reconstructions from results in panel A. (C) Feedbacks across various AGCMs, using the LGMR reconstruction of the LGM and $2xCO_2$ from LongRunMIP. (D) Mean and range of Δλ across various AGCMs from results in panel C. Note that HadGEM3 is not included in the kernel-derived feedbacks due to limited model output.

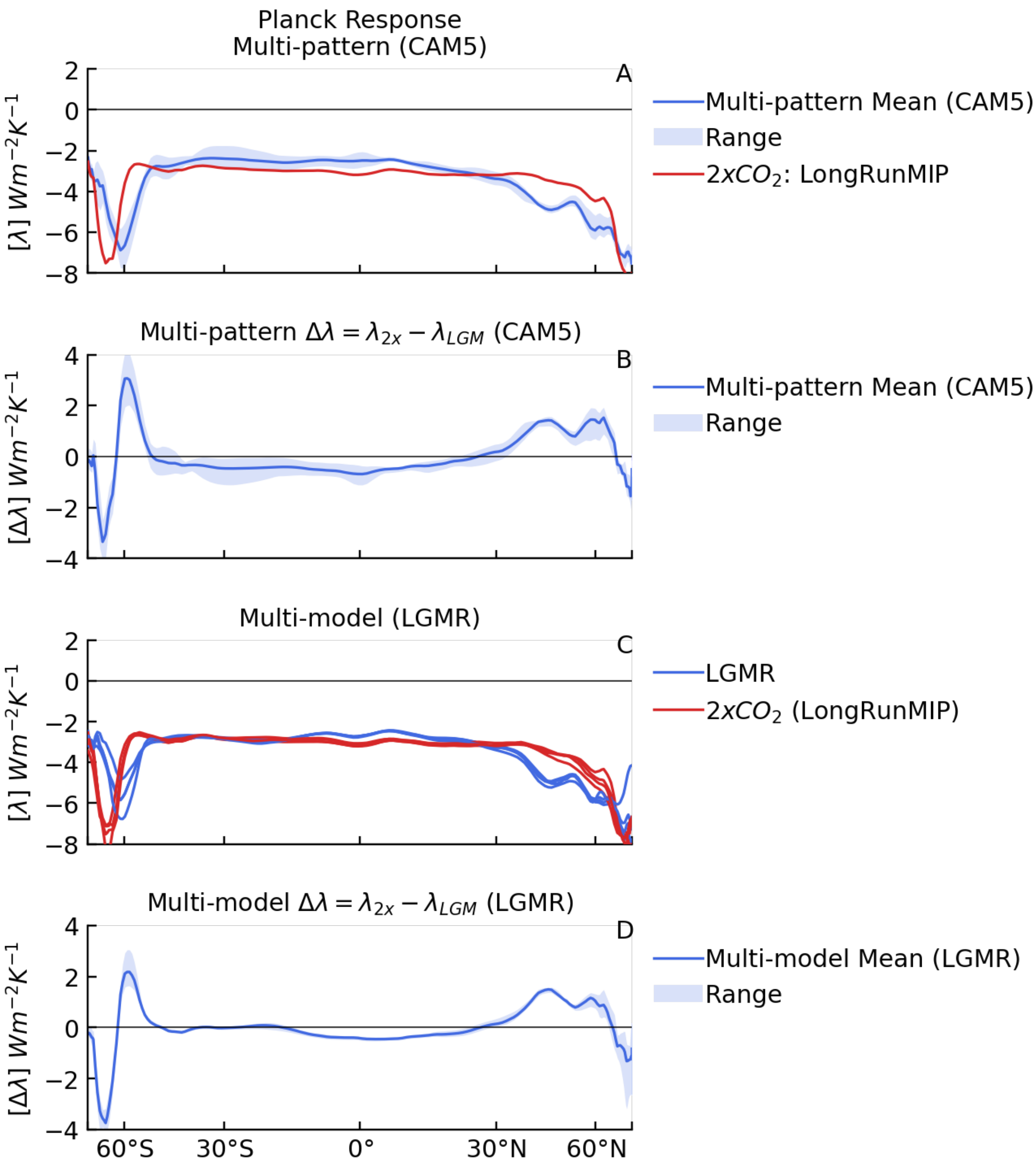

Figure S16. Zonal-mean Planck response and Δλ. (A) In CAM5, mean and range of feedbacks across four LGM reconstructions and $2xCO_2$ from LongRunMIP. (B) In CAM5, mean and range of the difference in feedbacks ($\Delta\lambda = \lambda_{2x} - \lambda_{LGM}$) across four LGM reconstructions from results in panel A. (C) Feedbacks across various AGCMs, using the LGMR reconstruction of the LGM and $2xCO_2$ from LongRunMIP. (D) Mean and range of Δλ across various AGCMs from results in panel C. Note that HadGEM3 is not included in the kernel-derived feedbacks due to limited model output.

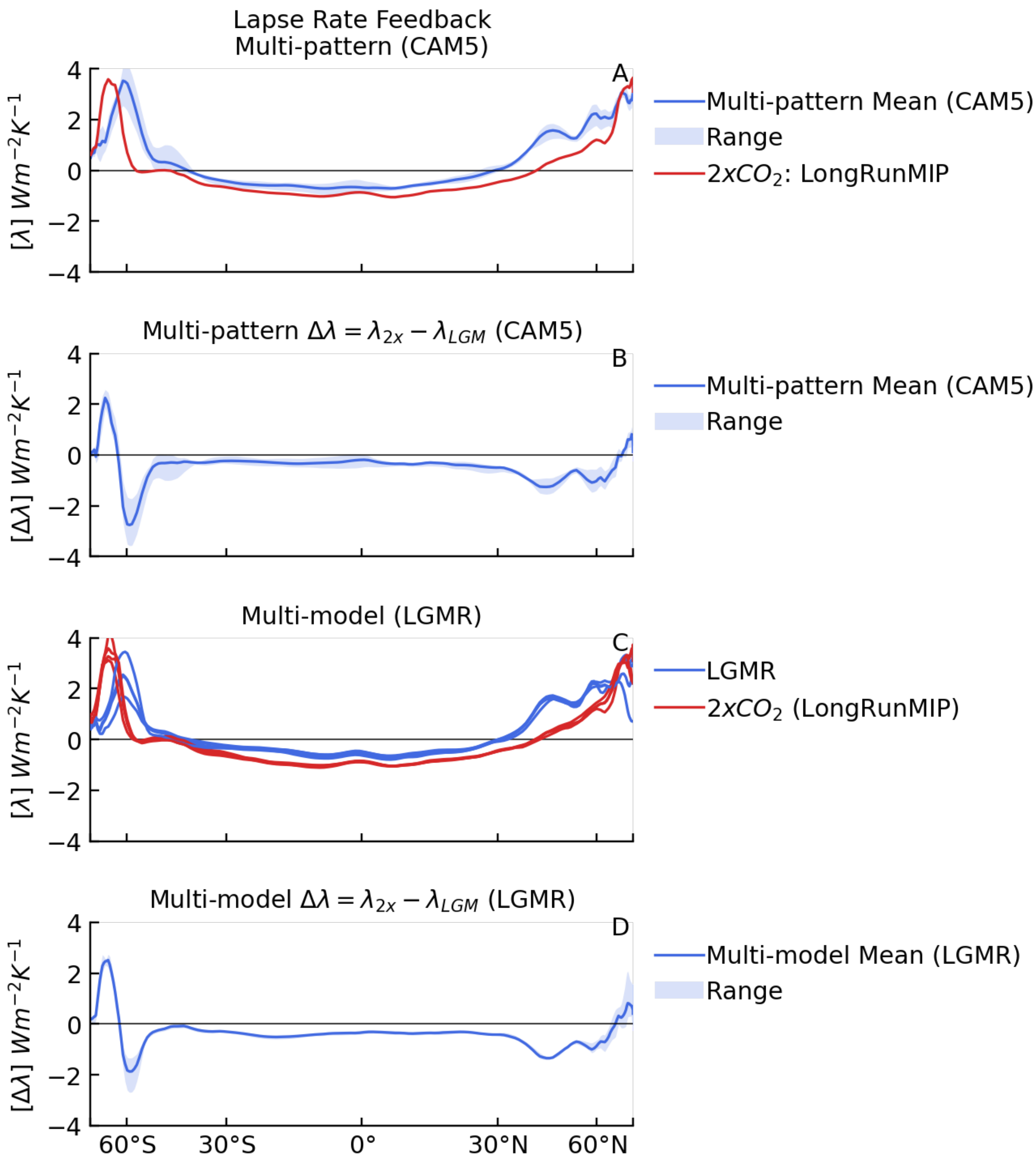

Figure S17. Zonal-mean lapse rate feedback and Δλ. (A) In CAM5, mean and range of feedbacks across four LGM reconstructions and $2xCO_2$ from LongRunMIP. (B) In CAM5, mean and range of the difference in feedbacks ($\Delta\lambda = \lambda_{2x} - \lambda_{LGM}$) across four LGM reconstructions from results in panel A. (C) Feedbacks across various AGCMs, using the LGMR reconstruction of the LGM and $2xCO_2$ from LongRunMIP. (D) Mean and range of Δλ across various AGCMs from results in panel C. Note that HadGEM3 is not included in the kernel-derived feedbacks due to limited model output.

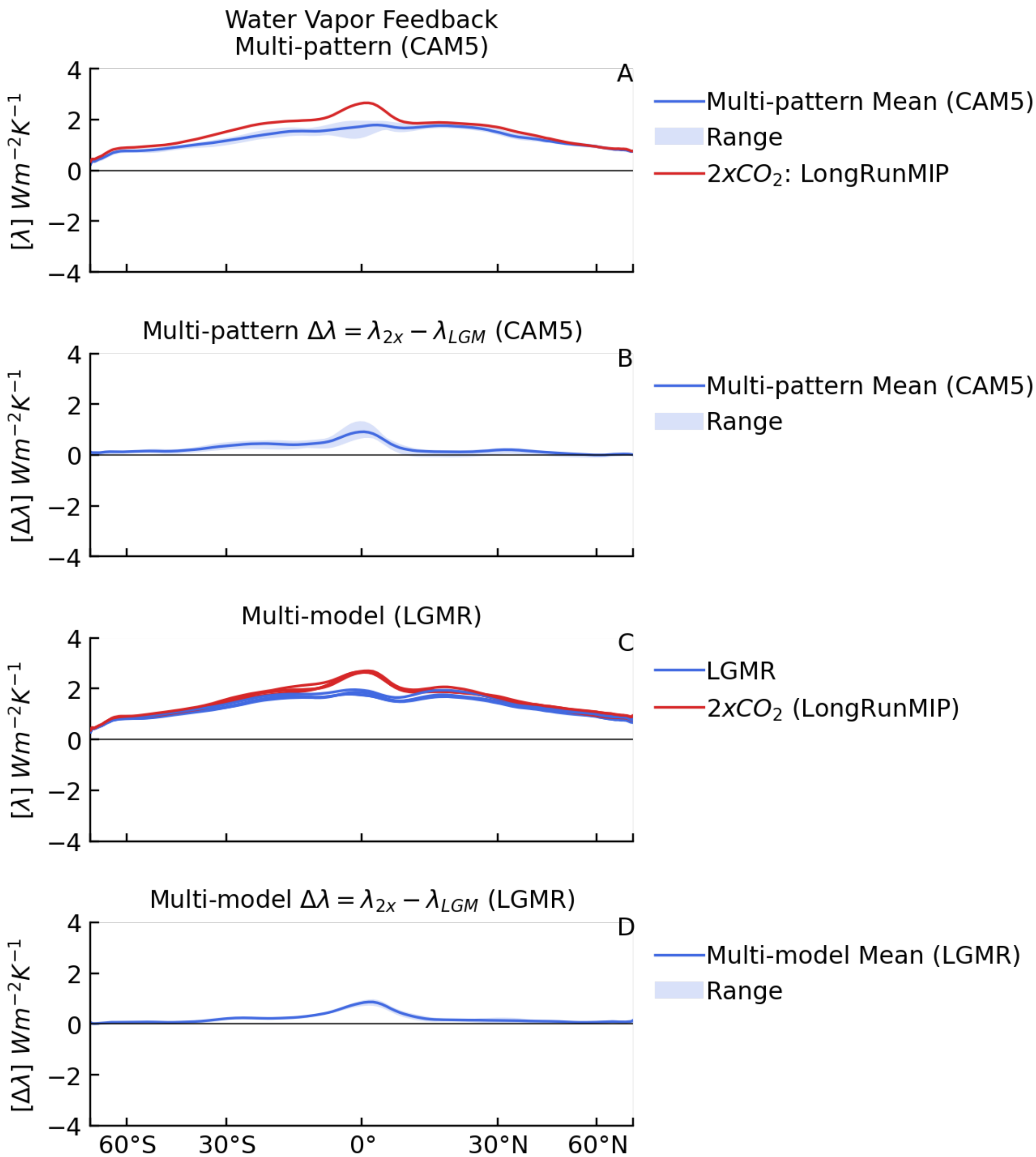

Figure S18. Zonal-mean water vapor feedback and Δλ. (A) In CAM5, mean and range of feedbacks across four LGM reconstructions and $2xCO_2$ from LongRunMIP. (B) In CAM5, mean and range of the difference in feedbacks ($\Delta\lambda = \lambda_{2x} - \lambda_{LGM}$) across four LGM reconstructions from results in panel A. (C) Feedbacks across various AGCMs, using the LGMR reconstruction of the LGM and $2xCO_2$ from LongRunMIP. (D) Mean and range of Δλ across various AGCMs from results in panel C. Note that HadGEM3 is not included in the kernel-derived feedbacks due to limited model output.

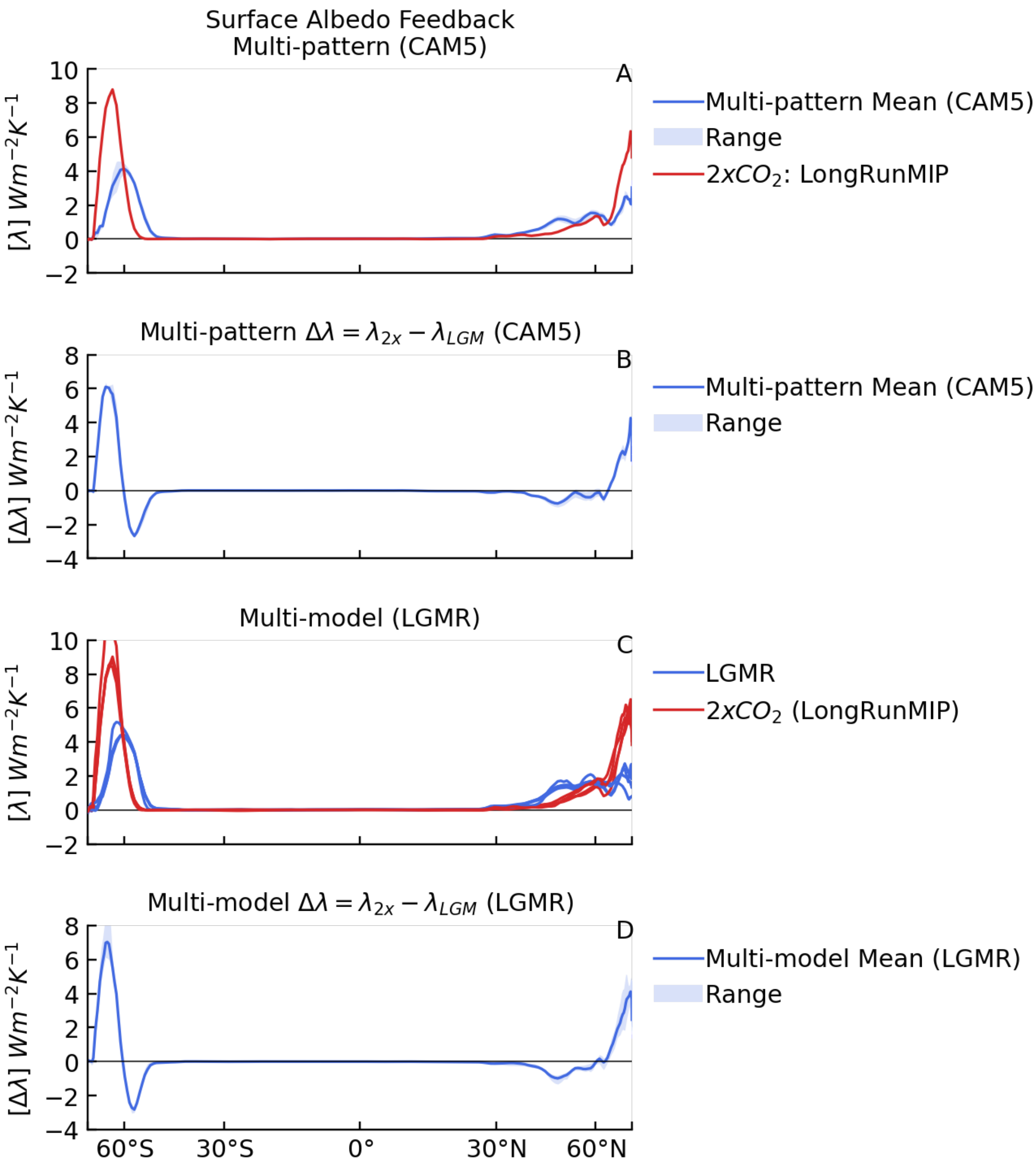

Figure S19. Zonal-mean surface albedo feedback and Δλ. (A) In CAM5, mean and range of feedbacks across four LGM reconstructions and $2xCO_2$ from LongRunMIP. (B) In CAM5, mean and range of the difference in feedbacks ($\Delta\lambda = \lambda_{2x} - \lambda_{LGM}$) across four LGM reconstructions from results in panel A. (C) Feedbacks across various AGCMs, using the LGMR reconstruction of the LGM and $2xCO_2$ from LongRunMIP. (D) Mean and range of Δλ across various AGCMs from results in panel C. Note that HadGEM3 is not included in the kernel-derived feedbacks due to limited model output.

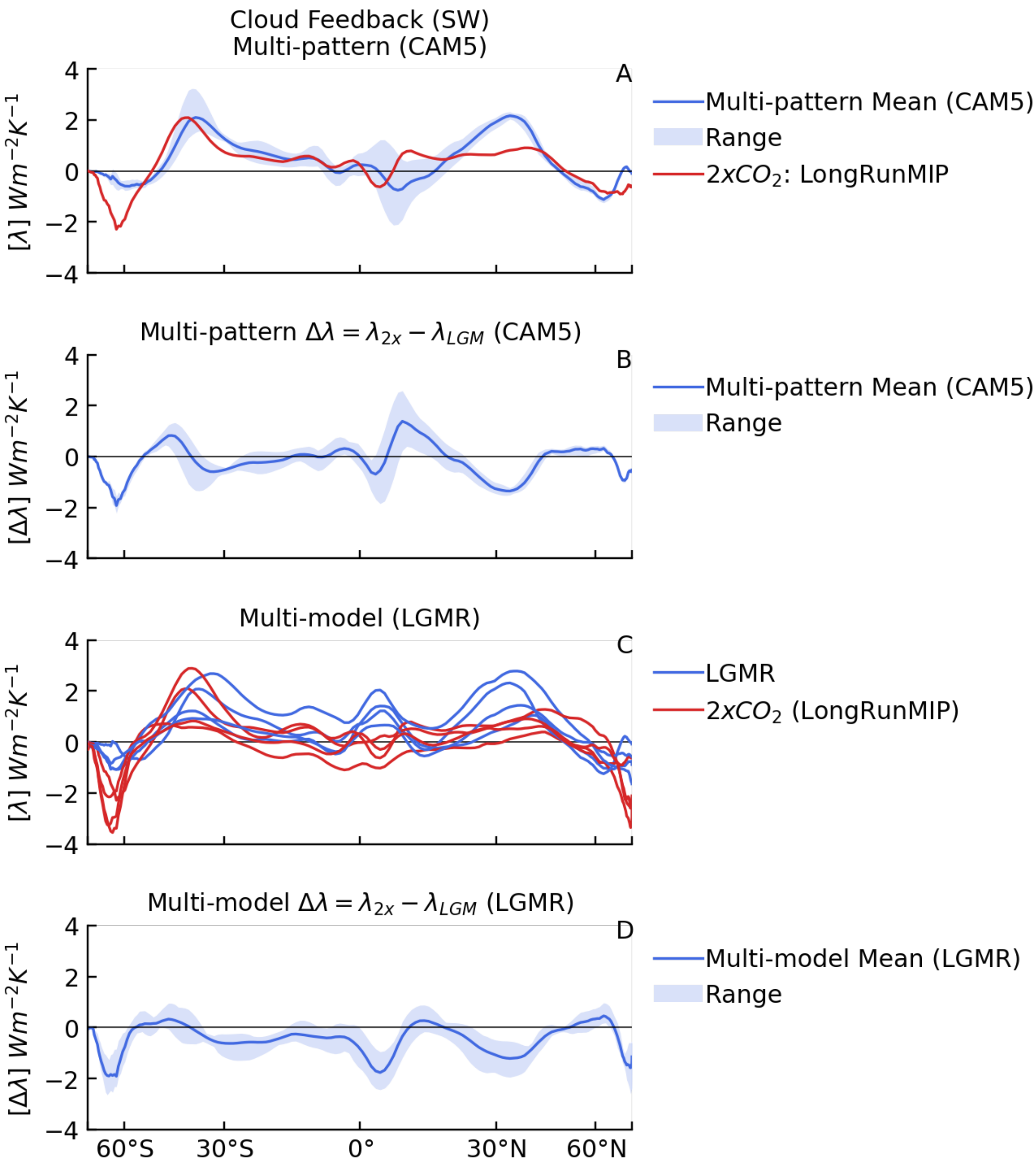

Figure S20. Zonal-mean shortwave cloud feedback and $\Delta\lambda$. (A) In CAM5, mean and range of feedbacks across four LGM reconstructions and $2xCO_2$ from LongRunMIP. (B) In CAM5, mean and range of the difference in feedbacks ($\Delta\lambda = \lambda_{2x} - \lambda_{LGM}$) across four LGM reconstructions from results in panel A. (C) Feedbacks across various AGCMs, using the LGMR reconstruction of the LGM and $2xCO_2$ from LongRunMIP. (D) Mean and range of $\Delta\lambda$ across various AGCMs from results in panel C. Note that HadGEM3 is not included in the kernel-derived feedbacks due to limited model output.

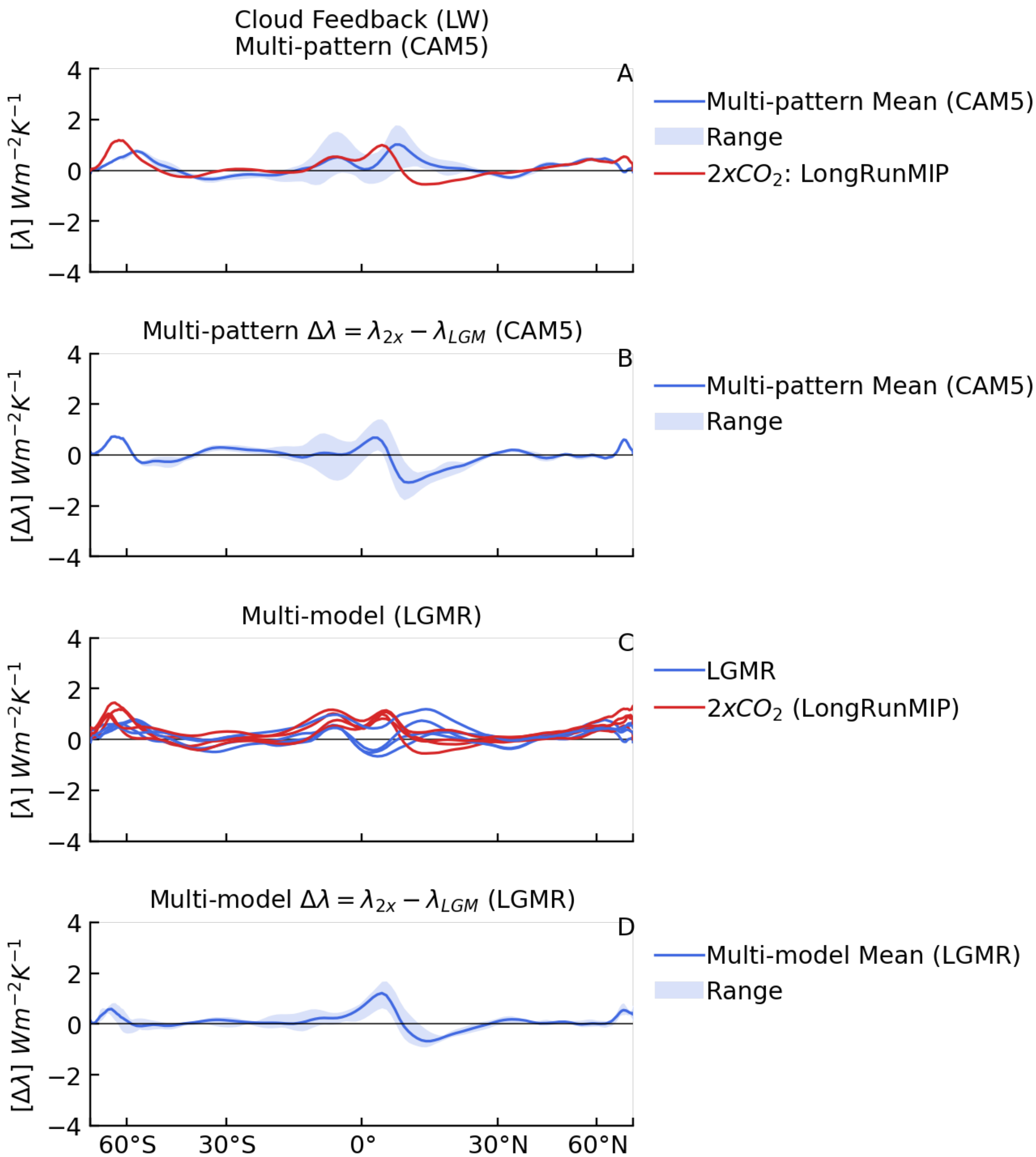

Figure S21. Zonal-mean longwave cloud feedback and Δλ. (A) In CAM5, mean and range of feedbacks across four LGM reconstructions and $2xCO_2$ from LongRunMIP. (B) In CAM5, mean and range of the difference in feedbacks ($\Delta\lambda = \lambda_{2x} - \lambda_{LGM}$) across four LGM reconstructions from results in panel A. (C) Feedbacks across various AGCMs, using the LGMR reconstruction of the LGM and $2xCO_2$ from LongRunMIP. (D) Mean and range of Δλ across various AGCMs from results in panel C. Note that HadGEM3 is not included in the kernel-derived feedbacks due to limited model output.

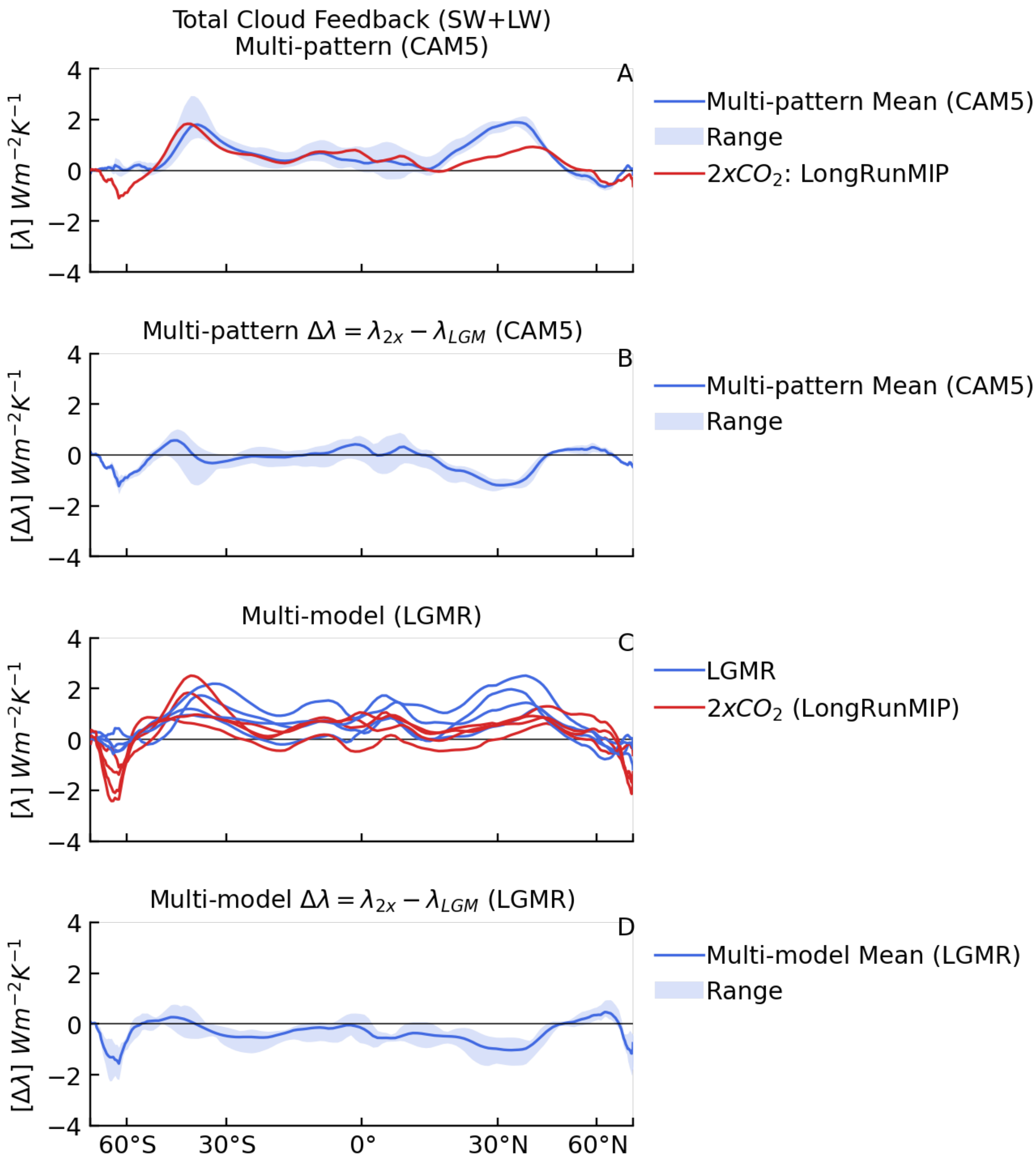

Figure S22. Zonal-mean total cloud feedback and Δλ. (A) In CAM5, mean and range of feedbacks across four LGM reconstructions and $2xCO_2$ from LongRunMIP. (B) In CAM5, mean and range of the difference in feedbacks ($\Delta\lambda = \lambda_{2x} - \lambda_{LGM}$) across four LGM reconstructions from results in panel A. (C) Feedbacks across various AGCMs, using the LGMR reconstruction of the LGM and $2xCO_2$ from LongRunMIP. (D) Mean and range of Δλ across various AGCMs from results in panel C. Note that HadGEM3 is not included in the kernel-derived feedbacks due to limited model output.

Table S1. LGM pattern effect and climate feedbacks in various AGCMs.

LGM pattern effect ($\Delta\lambda$) calculated as difference in net feedbacks (λ) from $2xCO_2$ and LGM. λ_{2x} is calculated in AGCM simulations with LongRunMIP (19) $2xCO_2$ pattern of SST/SIC. λ_{LGM} is calculated in AGCM simulations with LGMR (31) pattern. In two rightmost columns, alternative values for ($\Delta\lambda$) are shown using 150-year regression of abrupt-$4xCO_2$ from coupled models corresponding to each AGCM (43). ζ is assumed to be 0.06 based on WCRP20's central estimate (12).

[$Wm^{-2}K^{-1}$]	**$\Delta\lambda=\lambda_{2x}-\lambda_{LGM}$**	**λ_{2x}** LongRunMIP	**λ_{LGM}** LGMR	**$\Delta\lambda=\lambda_{4x(150yr)}/(1+\zeta)-\lambda_{LGM}$**	**$\lambda_{4x(150yr)}$**
CAM4	−0.45	−1.47	−1.02	−0.14	−1.23
CAM5	−0.31	−1.05	−0.74	−0.35	−1.15
CAM6	−0.63	−0.83	−0.19	−0.43	−0.66
GFDL-AM4	−0.33	−0.92	−0.60	−0.22	−0.86
HadGEM3-GC3.1-LL	−0.27	−0.62	−0.34	−0.25	−0.63
Mean	**−0.40**	**−0.98**	**−0.58**	**−0.28**	**−0.91**
Std. Dev.	*0.15*	*0.32*	*0.32*	*0.11*	*0.28*

Table S2. LGM pattern effect and climate feedbacks from various SST patterns.

LGM pattern effect ($\Delta\lambda$) from net feedbacks (λ) in $2xCO_2$ and with various LGM patterns of SST/SIC. λ_{2x} is calculated in AGCMs with LongRunMIP (19) $2xCO_2$ pattern of SST/SIC. λ_{LGM} is calculated in AGCM simulations with four LGM patterns. Global-mean anomalies for SST, near-surface air temperature (T), and top-of-atmosphere radiative imbalance (N) are shown for reference. Rightmost column shows values for LGM pattern effect using 150-year regression of abrupt-$4xCO_2$ from coupled models (43). ζ is assumed to be 0.06 based on WCRP20 central estimate (12).

	$\Delta\lambda=\lambda_{2x}-\lambda_{LGM}$ *$Wm^{-2}K^{-1}$*	**λ** *$Wm^{-2}K^{-1}$*	**$\Delta\overline{SST}$** *K*	**$\Delta\overline{T}$** *K*	**$\Delta\overline{N}$** *Wm^{-2}*	**$\Delta\lambda=\lambda_{4x(150yr)}/(1+\zeta)-\lambda_{LGM}$** *$Wm^{-2}K^{-1}$*
CAM4						
LGMR	−0.45	−1.02	−3.79	−5.06	5.14	−0.14
lgmDA	−0.69	−0.78	−3.14	−4.16	3.24	−0.38
Amrhein	−0.48	−0.99	−2.21	−3.38	3.36	−0.17
Annan	−0.29	−1.17	−2.18	−3.36	3.95	0.01
$Mean_{CAM4}$	**−0.48**	**−0.99**	**−2.83**	**−3.99**	**3.92**	**−0.17**
$StdDev_{CAM4}$	*0.16*	*0.16*	*0.78*	*0.80*	*0.87*	*0.16*
$2xCO_2$	—	*−1.47*	*2.35*	*3.08*	*−4.52*	—
CAM5						
LGMR	−0.31	−0.74	−3.79	−5.15	3.81	−0.35
lgmDA	−0.51	−0.54	−3.14	−4.24	2.27	−0.55
Amrhein	−0.33	−0.72	−2.21	−3.40	2.44	−0.37
Annan	−0.09	−0.97	−2.18	−3.38	3.28	−0.11
$Mean_{CAM5}$	**−0.31**	**−0.74**	**−2.83**	**−4.05**	**2.95**	**−0.34**
$StdDev_{CAM5}$	*0.18*	*0.18*	*0.78*	*0.84*	*0.72*	*0.18*
$2xCO_2$	—	*−1.05*	*2.35*	*3.09*	*−3.24*	—
$Mean_{CAM4\&5}$	**−0.39**	**−0.86**	**−2.83**	**−4.01**	**3.41**	**−0.26**
$StdDev_{CAM4\&5}$	*0.21*	*0.21*	*0.72*	*0.76*	*0.90*	*0.18*

Table S3. Climate feedbacks and temperature dependence from pattern-only simulations.

$\Delta\lambda_{PatternOnly}$ from pattern-only simulations, where LongRunMIP (19) 2xCO_2 and LGMR (31) patterns of SST anomalies are scaled to global-mean ΔSST of −0.5 K. Feedback dependence on global-mean temperature ($\Delta\lambda_T$) is estimated as the residual between Δλ in main simulations and $\Delta\lambda_{PatternOnly}$, i.e., assuming $\Delta\lambda=\Delta\lambda_{PatternOnly}+\Delta\lambda_T$. Note that total $\Delta\lambda=\lambda_{2x}-\lambda_{LGM}$.

Wm⁻²K⁻¹	$\lambda_{2x}^{-0.5K}$	$\lambda_{LGM}^{-0.5K}$	$\Delta\lambda_{Only}^{Pattern} = \lambda_{2x}^{-0.5K} - \lambda_{LGM}^{-0.5K}$	$\Delta\lambda_T = \Delta\lambda - \Delta\lambda_{Only}^{Pattern}$	$\Delta\lambda = \Delta\lambda_{Only}^{Pattern} + \Delta\lambda_T$, $\Delta\lambda = \lambda_{2x} - \lambda_{LGM}$
CAM4	−1.98	−1.55	−0.42	−0.03	−0.45
CAM5	−1.59	−1.24	−0.35	0.04	−0.31
CAM6	−1.30	−0.55	−0.75	0.12	−0.63
Mean	**−1.63**	**−1.12**	**−0.51**	**0.04**	**−0.47**

SI References

1. C. Zhou, *et al.*, Explaining Forcing Efficacy With Pattern Effect and State Dependence. *Geophys Res Lett* **50** (2023).
2. J. Hansen, *et al.*, Efficacy of climate forcings. *Journal of Geophysical Research: Atmospheres* **110**, 1–45 (2005).
3. J. D. Shakun, Modest global-scale cooling despite extensive early Pleistocene ice sheets. *Quat Sci Rev* **165**, 25–30 (2017).
4. J. Zhu, C. J. Poulsen, Last Glacial Maximum (LGM) climate forcing and ocean dynamical feedback and their implications for estimating climate sensitivity. *Climate of the Past* **17**, 253–267 (2021).
5. M. Yoshimori, T. Yokohata, A. Abe-Ouchi, A Comparison of Climate Feedback Strength between CO2 Doubling and LGM Experiments. *J Clim* **22**, 3374–3395 (2009).
6. M. Renoult, N. Sagoo, J. Zhu, T. Mauritsen, Causes of the weak emergent constraint on climate sensitivity at the Last Glacial Maximum. *Climate of the Past* **19**, 323–356 (2023).
7. J. Zhu, *et al.*, Assessment of Equilibrium Climate Sensitivity of the Community Earth System Model Version 2 Through Simulation of the Last Glacial Maximum. *Geophys Res Lett* **48** (2021).
8. L. B. Stap, P. Köhler, G. Lohmann, Including the efficacy of land ice changes in deriving climate sensitivity from paleodata. *Earth System Dynamics* **10**, 333–345 (2019).
9. J. Zhu, *et al.*, LGM Paleoclimate Constraints Inform Cloud Parameterizations and Equilibrium Climate Sensitivity in CESM2. *J Adv Model Earth Syst* **14**, e2021MS002776 (2022).
10. C. Zhou, M. D. Zelinka, S. A. Klein, Analyzing the dependence of global cloud feedback on the spatial pattern of sea surface temperature change with a Green's function approach. *J Adv Model Earth Syst* **9**, 2174–2189 (2017).
11. Y. Dong, C. Proistosescu, K. C. Armour, D. S. Battisti, Attributing Historical and Future Evolution of Radiative Feedbacks to Regional Warming Patterns using a Green's Function Approach: The preeminence of the Western Pacific. *J Clim* (2019) https:/doi.org/10.1175/JCLI-D-18-0843.1.
12. S. C. Sherwood, *et al.*, An Assessment of Earth's Climate Sensitivity Using Multiple Lines of Evidence. *Reviews of Geophysics* **58** (2020).
13. C. M. Bitz, *et al.*, Climate Sensitivity of the Community Climate System Model, Version 4. *J Clim* **25**, 3053–3070 (2012).
14. W. R. Peltier, D. F. Argus, R. Drummond, Space geodesy constrains ice age terminal deglaciation: The global ICE-6G-C (VM5a) model. *J Geophys Res Solid Earth* **120** (2015).
15. D. F. Argus, W. R. Peltier, R. Drummond, A. W. Moore, The Antarctica component of postglacial rebound model ICE-6G_C (VM5a) based on GPS positioning, exposure age dating of ice thicknesses, and relative sea level histories. *Geophys J Int* **198** (2014).
16. P. N. DiNezio, J. E. Tierney, The effect of sea level on glacial Indo-Pacific climate. *Nat Geosci* **6**, 485–491 (2013).
17. P. N. DiNezio, *et al.*, Glacial changes in tropical climate amplified by the Indian Ocean. *Sci Adv* **4** (2018).

18. J. W. Hurrell, J. J. Hack, D. Shea, J. M. Caron, J. Rosinski, A New Sea Surface Temperature and Sea Ice Boundary Dataset for the Community Atmosphere Model. *J Clim* **21**, 5145–5153 (2008).
19. M. Rugenstein, *et al.*, LongRunMIP: Motivation and Design for a Large Collection of Millennial-Length AOGCM Simulations. *Bull Am Meteorol Soc* **100**, 2551–2570 (2019).
20. P. R. Gent, *et al.*, The Community Climate System Model Version 4. *J Clim* **24**, 4973–4991 (2011).
21. A. Voldoire, *et al.*, Evaluation of CMIP6 DECK Experiments With CNRM-CM6-1. *J Adv Model Earth Syst* **11**, 2177–2213 (2019).
22. P. M. Cox, R. A. Betts, C. D. Jones, S. A. Spall, I. J. Totterdell, Acceleration of global warming due to carbon-cycle feedbacks in a coupled climate model. *Nature* **408**, 184–187 (2000).
23. T. Mauritsen, *et al.*, Developments in the MPI-M Earth System Model version 1.2 (MPI-ESM1.2) and Its Response to Increasing CO 2 Developments in the MPI-M Earth System Model version 1.2 (MPI-ESM1.2) and its response to increasing CO Journal of Advances in Modeling Earth Systems. *J Adv Model Earth Syst*, 11 (2019).
24. D. Paynter, T. L. Frölicher, L. W. Horowitz, L. G. Silvers, Equilibrium Climate Sensitivity Obtained From Multimillennial Runs of Two GFDL Climate Models. *Journal of Geophysical Research: Atmospheres* **123**, 1921–1941 (2018).
25. K-1 Model Developers, "K-1 Coupled GCM (MIROC) Description" (2004).
26. A. Yamamoto, *et al.*, Global deep ocean oxygenation by enhanced ventilation in the Southern Ocean under long-term global warming. *Global Biogeochem Cycles* **29**, 1801–1815 (2015).
27. J. M. Gregory, A new method for diagnosing radiative forcing and climate sensitivity. *Geophys Res Lett* **31**, L03205 (2004).
28. K. D. Williams, *et al.*, The Met Office Global Coupled Model 3.0 and 3.1 (GC3.0 and GC3.1) Configurations. *J Adv Model Earth Syst* **10**, 357–380 (2017).
29. I. M. Held, *et al.*, Structure and Performance of GFDL's CM4.0 Climate Model. *J Adv Model Earth Syst* **11**, 3691–3727 (2019).
30. D. E. Amrhein, G. J. Hakim, L. A. Parsons, Quantifying Structural Uncertainty in Paleoclimate Data Assimilation With an Application to the Last Millennium. *Geophys Res Lett* **47** (2020).
31. M. B. Osman, *et al.*, Globally resolved surface temperatures since the Last Glacial Maximum. *Nature* **599**, 239–244 (2021).
32. J. D. Annan, J. C. Hargreaves, T. Mauritsen, A new global surface temperature reconstruction for the Last Glacial Maximum. *Climate of the Past* **18**, 1883–1896 (2022).
33. A. G. Pendergrass, "CAM5 Radiative Kernels [Data set]" (2017) https:/doi.org/doi.org/10.5065/D6F47MT6.
34. A. G. Pendergrass, A. Conley, F. M. Vitt, Surface and top-of-atmosphere radiative feedback kernels for CESM-CAM5. *Earth Syst. Sci. Data* **10**, 317–324 (2018).
35. K. M. Shell, J. T. Kiehl, C. A. Shields, Using the Radiative Kernel Technique to Calculate Climate Feedbacks in NCAR's Community Atmospheric Model. *J Clim* **21**, 2269–2282 (2008).
36. P. Ceppi, J. M. Gregory, Relationship of tropospheric stability to climate sensitivity and Earth's observed radiation budget. *Proceedings of the National Academy of Sciences* **114**, 13126–13131 (2017).
37. M. D. Zelinka, *et al.*, Causes of Higher Climate Sensitivity in CMIP6 Models. *Geophys Res Lett* **47** (2020).
38. D. E. Amrhein, C. Wunsch, O. Marchal, G. Forget, A Global Glacial Ocean State Estimate Constrained by Upper-Ocean Temperature Proxies. *J Clim* **31**, 8059–8079 (2018).
39. J. E. Tierney, *et al.*, Glacial cooling and climate sensitivity revisited. *Nature* **584**, 569–573 (2020).
40. P. Forster, *et al.*, "2021: The Earth's energy budget, climate feedbacks, and climate sensitivity" in *Climate Change 2021: The Physical Science Basis. Contribution of Working Group I to the Sixth Assessment Report of the Intergovernmental Panel on Climate Change*, V. Masson-Delmotte, *et al.*, Eds. (Cambridge Univ. Press, 2021) https:/doi.org/10.1017/9781009157896.009.
41. J. Zhu, C. J. Poulsen, J. E. Tierney, Simulation of Eocene extreme warmth and high climate sensitivity through cloud feedbacks. *Sci Adv* **5** (2019).
42. B. J. Soden, I. M. Held, An Assessment of Climate Feedbacks in Coupled Ocean–Atmosphere Models. *J Clim* **19**, 3354–3360 (2006).
43. T. Andrews, *et al.*, On the Effect of Historical SST Patterns on Radiative Feedback. *Journal of Geophysical Research: Atmospheres* **127** (2022).